Science
AAAS

Supplementary Materials for

A framework for scintillation in nanophotonics

Charles Roques-Carmes *et al*.

Corresponding authors: Charles Roques-Carmes, chrc@mit.edu; Nicholas Rivera, nrivera@mit.edu

Science **375**, eabm9293 (2022)
DOI: 10.1126/science.abm9293

The PDF file includes:

Materials and Methods

Experimental

The electron-beam experiments were performed in a modified CamScan CS3200 custom Scanning Electron Microscope (SEM) from Applied Beams (Oregon). The electron emitter is a LaB6 emitter cathode operated with settings producing the highest currents (typically > 20 μA). Measurements are performed at the highest magnification (equivalent to spot mode). The sample is mounted on a 6-axis, fully eucentric stage, at a working distance of about 70 mm.

A Nikon TU Plan Fluor ×10 objective with a numerical aperture (NA) of 0.30 was used to collect light from the area of interest. The spectrometer used was an Acton SP-2360–2300i with a low-noise, deep-cooled PIXIS camera. Monochrome images of the radiation were collected with a Hamamatsu CCD, in order to align the optical setup and spatially resolve the observed radiation.

The objective is mounted on a 5-axis (XYZ, two tilt angles) homemade positioning stage. The focal spot of the objective is aligned with the electron beam focus (and sample surface). Two piezoelectric motors allow the objective to move in a plane parallel to the sample surface. A compact motorized actuator controls the distance of the objective to the sample surface. Two additional manual adjustment knobs allow control the alignment of the objective focal plane with the sample surface. The current is measured through a Faraday cup in the SEM stage, connected to a Keathley 6485 picoammeter. The picoammeter is triggered to acquire current signals during a time interval corresponding to the optical acquistion time (10 averaged acquisitions of 1 second duration, unless otherwise specified). A calibration measurement is performed with a calibrated light source of known power spectral density to convert the measured spectra to absolute power spectral densities and efficiencies. More information on the experimental setup can be found in the Supplementary Text, Section B. All spectra recorded with the spectrometers

were averaged over 10 acquisitions of 1 second each.

The x-ray experiments were carried out inside the enclosure of a ZEISS Xradia 520 Versa micro-CT machine. The same objective (Nikon TU Plan Fluor ×10) was mounted on the detector stage, and positioned to record an image of the surface of the scintillator. The scintillator and specimen were mounted on the same sample stage. Visible filters were taped directly at the back of the objective. In the images shown in Fig. 4 and 5 of the main text, no x-ray filters ("Air" setting) and a narrow bandpass visible filter (AVR Optics FF01-549-15-25) were used. Additional data showing the influence of visible and x-ray filters is given in the Supplementary Text, Section H.

The sample wafer for electron-beam-induced scintillation was purchased from MEMS Material and Engineering, Inc. (Sunnyvale, CA). The wafer was fabricated by a fusion bonding - grinding - polishing process. The wafer is made of a device layer (p-doped polished silicon, $\langle 100 \rangle$ orientation, resistivity 1-30 Ω.cm, thickness 0.5 $\pm$ 0.025 μm), on top of an oxide layer (amorphous silica, thickness 1.0 μm $\pm$ 5%), on top of a handle wafer (p-doped silicon, $\langle 100 \rangle$ orientation, resistivity 1-30 Ω.cm, thickness 625 $\pm$ 10 μm). The patterning was produced by Dr. Timothy Savas with optical interference lithography. The YAG:Ce crystal used in the x-ray experiment was purchased from Crytur and patterned with a VELION FIB-SEM. Fabrication parameters are given in the Supplementary Text, Section H. One reason we employed the VELION FIB-SEM is that nanofabrication techniques to pattern YAG:Ce are limited. Another reason is that the VELION's FIB field has astigmatism and distortion corrections, enabling more accurate large-area FIB patterning. Finally, we selected the Au^+ FIB because it conveniently matched the Au later that would subsequently be removed with Au selective etchant.

Fitting to experiments

The experimentally obtained spectra in Fig. 2D of the main text were accounted for based on Eq. 1 of the main text. The red and green peaks of STH were separately fitted (hence, no assumption is made about the relative oscillator strengths of the two peaks). The spectral dependence of $S(\mathbf{r}, \omega)$ was taken as a sum of two Gaussians at the red and green peaks, on account of inhomogeneous broadening of the defect levels. Fits were obtained taking the red and green peak energies to be 1.95 and 2.6 eV respectively, with respective FWHM of 0.25 eV and 1.2 eV. Both the peak energies and widths are consistent with previous experimental measurements of STH spectra (*40*), as well as with our DFT calculations. The function V_{eff}, as defined in Fig. 1 of the main text is calculated using rigorous coupled-wave analysis.

The function $V_{\text{eff}}^{(i)}(\omega, \Omega)$ is calculated through the volume-integrated field enhancement of a plane wave incident from the far-field at angles $\Omega = (\theta, \phi)$ with polarization $i \in \{s, p\}$ and frequency ω. The integration volume (particularly, the effective depth inside silica) is fitted to provide a good agreement with experiment, and accordingly the integrand of V_{eff} is integrated to a depth of 500 nm inside the silica layer, which is within a factor of 2 of the effective depth predicted from CASINO and is within the uncertainty of the incident angle of the electron beam. The theoretically predicted signals are averaged over the numerical aperture of the objective (17.5°) and summed over polarizations. The data is best explained assuming that the samples have a small ($\sim 8°$) misalignment of their normal to the axis of the objective, with the 25 nm sample oppositely oriented from the other samples. The data used for the fit was not normalized by the incident current. Given the moderate variations in currents from sample to sample, similarly good fits can be obtained with the current-normalized data.

For the x-ray experiments: absorption maps are calculated with rigorous coupled-wave analysis, with geometrical parameters extracted from SEM/AFM measurements. The reported value of the loss in the unpatterned YAG:Ce film is of $\text{Im}(\epsilon) \sim \times 10^{-6}$ (information provided by Cry-

tur). Geometrical parameters are extracted via an atomic force microscopy measurement fitted to as $\sin^2$ profile. Error bars on the predicted enhancements are calculated by varying the geometrical parameters according to the measured error bars from the characterization.

Monte Carlo HEP Energy Loss Simulations

HEP energy loss was calculated for energetic free-electrons impinging on the (unpatterned) silicon-on-insulator wafer using the open source CASINO Monte Carlo software. Calculations of the position-dependent energy loss density, $\frac{dE}{dV}(x, y, z)$ were done for electrons incident at shallow angles of incidence ($\sim 1^\circ$ measured with respect to the substrate plane) by averaging over results from 250,000 incident electrons. The data was used to calculate the marginal electron energy loss distribution per depth $\frac{dE}{dz} = \int dxdy \, \frac{dE}{dV}$ shown in Fig. 2B of the main text. We note that these calculations were also used to model scintillation in patterned samples, thus effectively neglecting the influence of the shallow pattern on the electron energy loss map.

Calculations were also performed to find the energy loss density as a function of the incident electron energy, which was used as input in the fits of Fig. 3E of the main text. Similar calculations were also done for predictions of enhanced luminescence of boron nitride in the Supplementary Text, Section F.

Density Functional Theory (DFT) Calculations

DFT calculations (*61, 62*) were performed on one bulk and three cluster models of STH. Cluster calculations used the Boese-Martin exchange correlation functional with 42% exact exchange (*63*) to take into account self-interaction effects. Dangling bonds were passivated with hydrogen atoms to mitigate their effect on the electronic structure. A 20 Hartree plane wave cutoff was used and Coulomb truncation (*64*) was implemented to mitigate the effects of cluster-cluster interactions. The defect transitions observed were attributed to localized states at the oxygen

atoms – verified by calculations of the spin density.

Bulk models, shown in Fig. 3 of the main text, with constrained 1 Bohr/unit cell magnetization yielded trapped hole defects without the need for hybrid functionals. These models yielded the same transition energies as above but used the PBE exchange correlation functional (*65*). Additional details on the various DFT models and calculation results are shown in the Supplementary Text, Section G.

Three-level rate equation model

Based on DFT calculations, a simplified three-level system is designed to model electron pumping and subsequent radiative emission from defect states in silica. The model is pictured in Fig. 3C of the main text, corresponding to calculated energy levels from the DFT model in Fig. 3A. The following rate equations are used to model the system:

$$\begin{cases} \frac{dp_1}{dt} = & -\Gamma_{13}\, p_1(1-p_3) + \Gamma_{31}\, p_3(1-p_1) \\ \frac{dp_2}{dt} = & -\Gamma_{23}\, p_2(1-p_3) + \Gamma_{32}\, p_3(1-p_2) \\ \frac{dp_3}{dt} = & \Gamma_{13}\, p_1(1-p_3) - \Gamma_{31}\, p_3(1-p_1) \\ & +\Gamma_{23}\, p_2(1-p_3) - \Gamma_{32}\, p_3(1-p_2) \end{cases} \tag{1}$$

such that the total occupation number is conserved over time $\frac{d\sum_i p_i}{dt} = 0$ with the initial condition $p_1 = p_2 = 1$ and $p_3 = 0$. This set of equations describe a three-level system, where 1 (resp. 2) is the ground state corresponding to green (resp. red) emission, 3 is a shared excited state to which electrons are sent via free-electron pumping. Band electrons can relax from the excited state 3 to one of two ground states 1 and 2, corresponding to the green and red peak emission, respectively.

We can solve the steady-state of Eq. 1 to estimate the ratio of green to red emission at the steady-state:

$$\eta = \frac{\Gamma_{31}\,(1-p_1)}{\Gamma_{32}\,(1-p_2)}. \tag{2}$$

Calculations were performed using the DifferentialEquations.jl package in Julia (*66*) and fitted using the LsqFit.jl package.

We use this model to gain further microscopic understanding of the observed experimental data, in conjunction with the general nanophotonic scintillator theory described in the main text. We chose η as an experimental observable, since it can be calculated from Eq. 1 and – assuming green and red peak defects are localized in the same region – the observable is independent of a few experimental unknowns (beam size, number of excited emitters). Electrons in state 3 can then radiatively decay into state 1 or 2.

We assume that Γ is proportional to the electron beam energy deposited in the luminescent material: $\Gamma \propto I \times E \times \eta_{\text{ene}}(E)$ where I is the incident electron current, E its kinetic energy (in keV), and $\eta_{\text{ene}}(E)$ the fraction of energy (normalized to the incident energy E) deposited by an electron in the silica layer, calculated via Monte-Carlo Simulations of electron scattering in the TF sample (see corresponding Methods section above "Monte Carlo HEP Energy Loss Simulations").

In a first numerical experiment shown in Fig. 3E of the main text, we utilized scintillation data measured on the TF sample at various incident voltages and currents. This data was used to estimate the ratio of pumping rates $\Gamma_{13}/\Gamma_{23} = 3.2 \pm 0.09$. This value indicates an intrinsic preference of the system to excite the green defect through electron pumping.

In a second numerical experiment shown in Fig. 3E of the main text, we utilized scintillation data measured on the PhC sample at various incident voltages and currents. This data was used to estimate the ratio of decay rates enhancements Γ_{32}/Γ_{31} and to confirm the value of Γ_{13}/Γ_{23}. When letting both parameters be optimized, we obtain a value of $\Gamma_{13}/\Gamma_{23} = 3.35 \pm 0.13$, similar to the original value. We can also estimate the value of $\left(\frac{\Gamma_{32}}{\Gamma_{31}}\right)_{\text{PhC}} \left(\frac{\Gamma_{32}}{\Gamma_{31}}\right)_{\text{TF}}^{-1} \sim 2.3$ which corresponds to the scintillation rate enhancement of the red defects. This value is in agreement with our calculations and experimental demonstration of V_{eff} scintillation enhancement of the

red defects. The relative error of this estimate is of ± 0.4 (uncertainty coming from the first numerical experiment) and of ± 0.9 (uncertainty coming from the second numerical experiment). Therefore, results from the three-level model are a strong indication of the microscopic nature of the observed scintillation spectrum.

We verified the robustness of our fits by trying different differential equation solvers and fitting methods, and did not observe any significant change in the values obtained for the parameters of interest, which indicates the consistency of our approach. For instance, another local optima of the optimization, which we did not detail for the sake of brevity, had the following parameters: $\Gamma_{13}/\Gamma_{23} = 4.43 \pm 0.94$ (TF data only), $\Gamma_{13}/\Gamma_{23} = 4.42 \pm 0.17$ (PhC data only), and $\left(\frac{\Gamma_{32}}{\Gamma_{31}}\right)_{\text{PhC}} \left(\frac{\Gamma_{32}}{\Gamma_{31}}\right)_{\text{TF}}^{-1} \sim 4.06$, with relative error of this estimate of ± 1.42 (uncertainty coming from the second numerical experiment) and of ± 7.15 (uncertainty coming from the first numerical experiment). Though the error bar in Fig. 3 of the main text only shows the relative model uncertainty with respect to the value of $\frac{\Gamma_{32}}{\Gamma_{31}}$ (which is the main decay rate variable relating to our experimental observables), we observe that the relative error of other parameters is comparable or lower.

Supplementary Text

Section A: End-to-end framework summarized

In this section, we provide additional details about our end-to-end framework to model scintillation in nanophotonics, shown in Fig. **S1**, and summarized in Fig. 1G of the main text.

Our framework is fed inputs, which specify the scintillating material, the high energy particle, and the electromagnetic properties of the nanophotonic environment. For example, the scintillating material might be specified by its atomic number and relevant defect/dopant concentrations (if the scintillation is from defects/dopants, as in both cases we consider in the main text). The high-energy particle (HEP) would be specified by the type of particle, as well as its angle of incidence and energy. And the nanophotonic structure is specified by the spatially varying permittivity of the system.

These inputs are transformed into outputs by the following simulation components:

1. **Monte Carlo HEP energy loss** calculations are performed to calculate the three-dimensional energy loss per unit volume (energy loss density) of the HEPs through the structure. Radiative sites may diffuse before emitting, as is typically the case for electron-hole pairs in semiconductors, in which case carrier diffusion may be taken into account at this stage. This energy loss is proportional to the density of excited electrons that ultimately scintillate. This energy loss information can be further combined (as we do in Fig. 3 of the main text) with rate equations to calculate occupation factors of various scintillating levels.

2. **Density Functional Theory (DFT)** is used to calculate the scintillation emitter energy levels and oscillator strengths, which feed into the calculation of the spectral function.

3. **Full-wave nanophotonics simulations** are performed to calculate the position-dependent field enhancement in the nanophotonic structure, where the incident field is taken as a

plane wave incident at some given angles, frequency, and polarizations. The field enhancement is integrated over space, weighted by the position-dependent spectral function (which depends on the spatially-dependent occupation factors).

In principle, these steps are coupled together: the field enhancement is set by the density of excited electrons created by HEPs, and, if their density is high enough, it would change the field solutions relative to the case of no excited electrons. This is because this density of excited electrons can be seen as a change to the permittivity of the scintillator. Thus, the truly *ab initio* method would be to (1) evaluate the position-dependent energy loss density by HEPs, (2) translate this into a density of excited electrons, and (3) calculate the electromagnetic field enhancement of incident plane-waves sent into a material with a permittivity taking these excited electrons into account. In cases we consider, it is adequate to approximate the excited electrons as only weakly changing the permittivity of the scintillator, thus allowing us to decouple the energy-loss and nanophotonic calculations.

Coupled together, results from these three methods allow us to calculate the effective absorption volume (via electromagnetic reciprocity) and the non-equilibrium occupation function. Plugging these two into our theory enables us to calculate the scintillation signal and its polarization, spectral, and angular dependence (as in Eq. 1 from the main text). Alternatively, our framework allows us to calculate the scintillation power density by integrating the spatially-varying effective field enhancement and non-equilibrium occupation over the scintillating volume.

Beyond using this framework to predict the scintillation spectrum, we can also use it to optimize or inverse design the scintillation (e.g., for maximum photon yield, directivity, etc.). This step requires differentiability of the inputs, which for now is only the case for the full-wave nanophotonics, in which case we treat the energy loss as fixed. More details about the inverse design of nanophotonic scintillators, enabled by our framework, can be found in Section E.

Section B: General nanophotonic theory of scintillation

In this section, we develop a general quantitative framework for describing scintillation in nanophotonics, providing additional details on the derivation of Equations (1) and (2) of the main text. Let us consider, as in Fig. 1 of the main text, a material with scintillating centers. Such scintillating centers can be associated with defects or dopants in materials (as in the case of what we consider in the experiments of the main text), electron-hole recombination in semiconductors, excitons, or other mechanisms. Such centers can be generated optically, as in photoluminescence, or via a beam of HEPs, such as electrons (incoherent cathodoluminescence), x-rays, γ-Rays, radioactive particles, and cosmic rays. In all cases, the spontaneous emission associated with these emitters can be considered as a type of non-equilibrium radiation from fluctuating currents of current density $\mathbf{J}(\mathbf{r},\omega)$ in the material. The correlation functions of the current, of the form $\langle J_j(\mathbf{r},\omega)J_k(\mathbf{r}',\omega)\rangle$ (with j,k labeling vector components) are determined by the microscopic structure of the scintillating center (the energy levels and current matrix elements), as well as the non-equilibrium occupation of the various energy levels. These occupation functions depend on the pump strength, and are inferred via a combination of Monte Carlo simulations and a kinetic model of the transition dynamics of the electron between energy levels. As a point of notation, we index the energy levels by the label α, with corresponding energy $E_\alpha \equiv \hbar\omega_\alpha$ and occupation factor f_α.

In what follows, we will take advantage of the fact that in many cases of interest in scintillation, there is a separation of time scales between: (1) the processes that create the excited scintillation centers, and (2) the recombination that leads to radiation. In particular, the process of impact ionization of an electron, followed by relaxation (e.g., by phonons and electron-electron scattering) to the lowest unoccupied states of the system, occurs on timescales much shorter than the spontaneous emission. The spontaneous emission, in many systems, occurs on timescales between microseconds and nanoseconds. As a result of this, we can approximate the

scintillating system as being in a non-equilibrium *steady state*, and so the occupation functions − which govern the correlation functions of the fluctuating current − remain well-defined. In that case, the normally-ordered correlation function between different components of the current is given simply as

$$\langle J_j^-(\mathbf{r}_1,\omega)J_k^+(\mathbf{r}_2,\omega)\rangle = 2\pi T\sum_{\alpha,\beta} J_j^{\alpha\beta}(\mathbf{r}_1)J_k^{\beta\alpha}(\mathbf{r}_2)f_\alpha(1-f_\beta)\delta(\omega-\omega_{\alpha\beta}) \equiv 2\pi T S_{jk}(\mathbf{r_1},\mathbf{r}_2,\omega). \tag{3}$$

where T a normalization time and $J_k^{\alpha\beta}(\mathbf{r})$ is the matrix element of the k-component of the current density operator between quantum states α and β. Further note that we have taken the correlation function between the negative $(-)$ and positive $(+)$ frequency parts of the current operator, as the far-field flux depends on this combination of current operators. The radiated intensity spectrum in the far-field, along the ith polarization, $\frac{dI^{(i)}(\mathbf{r})}{d\omega}$ which is given in terms of the normally-ordered correlation functions of the electric fields, is (in repeated index notation for j,k)

$$\frac{dI^{(i)}(\mathbf{r})}{d\omega} = \frac{2\mu_0\omega^2}{c}\int d\mathbf{r_1}d\mathbf{r_2}\; G_{ij}^*(\mathbf{r},\mathbf{r}_1,\omega)G_{ik}(\mathbf{r},\mathbf{r}_2,\omega)S_{jk}(\mathbf{r}_1,\mathbf{r}_2,\omega). \tag{4}$$

Here, the Green's function $G_{ij}(\mathbf{r},\mathbf{r}_1,\omega)$ is the ith component of the electric field at the position $\mathbf{r}$ created by a dipole at location $\mathbf{r}_1$ and oriented along direction j. What we will now show is that the scintillation spectrum is directly related to the field enhancement in the scintillation volume, which is also proportional to the absorption in the scintillation volume (provided that the absorption is sufficiently weak as to not change the field solutions). Let us focus on the widely applicable case in which the current fluctuations are *local*, so that $S_{jk}(\mathbf{r}_1,\mathbf{r}_2,\omega) = S_{jk}(\mathbf{r}_1,\omega)\delta(\mathbf{r}_1-\mathbf{r}_2)$. We note that in a bulk medium, S would need to be translationally invariant, and this can be taken to be the case either for homogeneously distributed defects or a bulk solid. However, we also note that in cases we consider, due to the spatial non-uniformity of the pump, the occupation factors can depend on position (over a length scale typically much larger than the electronic

length-scale), so that $f_{\alpha,\beta} \to f_{\alpha,\beta}(\mathbf{r})$.

In the case described above, we have

$$\frac{dI^{(i)}(\mathbf{r})}{d\omega} = \frac{2\mu_0\omega^2}{c}\int d\mathbf{r_1}\; G^*_{ij}(\mathbf{r},\mathbf{r}_1,\omega)G_{ik}(\mathbf{r},\mathbf{r}_1,\omega)S_{jk}(\mathbf{r}_1,\omega). \tag{5}$$

In reciprocal electromagnetic systems, $G_{ij}(\mathbf{r},\mathbf{r}_1,\omega) = G_{ji}(\mathbf{r}_1,\mathbf{r},\omega)$, thus relating the power to the field emitted by a dipole at position $\mathbf{r}$, which is taken to be in the far-field. Let us define $G_{ji}(\mathbf{r}_1,\mathbf{r},\omega) = \alpha E^{(i)}_j(\mathbf{r}_1,\mathbf{r},\omega)$, with α a proportionality factor, and $E^{(i)}_j(\mathbf{r}_1,\mathbf{r},\omega)$ the electric field along component j at position $\mathbf{r}_1$ created by a dipole located at position $\mathbf{r}$ and polarized along direction i (and at frequency ω). Then, Eq. 5 can thus be translated into the i-polarized power spectrum per unit solid angle $\frac{dP^{(i)}}{d\omega d\Omega}$ as:

$$\frac{dP^{(i)}}{d\omega d\Omega} = \frac{\omega^2}{8\pi^2\epsilon_0 c^3}\int d\mathbf{r}'\frac{E^{*(i)}_j(\mathbf{r}',\mathbf{r},\omega)}{\left|\mathbf{E}^{(i)}_{\text{inc}}(\mathbf{r}',\mathbf{r},\omega)\right|}\frac{E^{(i)}_k(\mathbf{r}',\mathbf{r},\omega)}{\left|\mathbf{E}^{(i)}_{\text{inc}}(\mathbf{r}',\mathbf{r},\omega)\right|}S_{jk}(\mathbf{r}',\omega), \tag{6}$$

where we have defined $|\mathbf{E}^{(i)}_{\text{inc}}(\mathbf{r}',\mathbf{r},\omega)|$ as the magnitude of the field of a dipole with polarization i at frequency ω, emitting from the far-field, which is $|\alpha|/4\pi|\mathbf{r}-\mathbf{r}'|$. The unpolarized spectrum is simply obtained by summing over i. Since the scintillating material is far from the detector, this field is equivalent to a plane wave incident from the far field at an angle set by $\mathbf{r}$. Thus, we may rewrite the various fields more simply as $\mathbf{E}(\mathbf{r}',\mathbf{r},\omega) \to \mathbf{E}(\mathbf{r}',\omega,\Omega)$, with Ω denoting a direction about which an infinitesimal solid angle $d\Omega$ is centered. While this result is general, to make clear the physics contained within Eq. 6, we consider the case where the scintillating material is isotropic, so that $S_{jk}(\mathbf{r}',\omega) = \delta_{jk}S(\mathbf{r}',\omega)$. In that case, also using the simplified notation of this paragraph, we have

$$\frac{dP^{(i)}}{d\omega d\Omega} = \frac{\omega^2}{8\pi^2\epsilon_0 c^3}\int d^3\mathbf{r}\frac{\left|\mathbf{E}^{(i)}(\mathbf{r},\omega,\Omega)\right|^2}{\left|\mathbf{E}^{(i)}_{\text{inc}}(\omega,\Omega)\right|^2}S(\mathbf{r},\omega). \tag{7}$$

Here, we have also taken $\mathbf{r}' \to \mathbf{r}$ in the integration. We have also used the fact that, since the incident field looks like a plane wave in the far-field limit, its norm is position-independent. This equation coincides with Equation (1) of the main text.

From Eq. 7, one can immediately see that the emitted power is proportional to the field enhancement by a plane wave at frequency ω, direction Ω, and polarization i inside the volume governed by the scintillating material. This is also proportional to the absorbed power of the plane wave. In particular, if instead of S, one had Im ϵ, then Eq. 7 would be directly proportional to the absorbed power. In fact, the spectral function computed here is proportional to (up to a frequency-dependent factor) the dielectric function corresponding to the material being in a non-equilibrium steady-state with the same occupation functions. As a reminder, the spectral function $S(\mathbf{r}, \omega)$ is set by microscopic properties of the material (energy levels, current/dipole matrix elements), and the properties of the pump beam (current, energy), the latter of which sets the spatial distribution of S through the occupation functions. Therefore, for a fixed pump, maximizing scintillation corresponds directly to maximization of the absorbed power / field enhancement in the volume set by the distribution of scintillating material.

We note that similar considerations based on electromagnetic reciprocity have been utilized to make predictions in other areas of non-equilibrium radiation,such as thermal radiation, LEDs, and generalizations of the Purcell effect to non-equilibrium bodies (*34, 49–51*).

It is worthwhile to take a few additional simplifying assumptions that lead to an extremely simple formula for scintillation. Consider the case where S is effectively independent of position in the scintillation volume V_S (and its spatial dependence may be dropped so that $S(\mathbf{r}, \omega) \to S(\omega)$). In that case, we may write

$$\frac{dP^{(i)}}{d\omega d\Omega} = \frac{\pi}{\epsilon_0 \omega} \times S(\omega) \times (V_{\text{eff}}^{(i)}(\omega, \Omega)/\lambda^3), \tag{8}$$

where $V_{\text{eff}}^{(i)}(\omega)$ is the effective volume of absorption or field enhancement (note that it has dimensions of volume) – defined by $V_{\text{eff}}^{(i)}(\omega, \Omega) = \int_{V_S} d\mathbf{r} \; |\mathbf{E}^{(i)}(\mathbf{r}, \omega, \Omega)|^2 / |\mathbf{E}_{\text{inc}}^{(i)}(\omega, \Omega)|^2$ – and $\lambda = 2\pi c/\omega$. Such an expression states that the scintillation spectrum is a simple product of a microscopic factor, set by the non-equilibrium steady-state distribution function, and an effec-

tive absorption volume, which is set only by the (structured) optical medium surrounding the scintillating medium. This expression also allows inference of the microscopic spectral function $S(\omega)$, given the knowledge of V_{eff}, and a measurement of the scintillation spectrum.

As a simple example of V_{eff} which can be calculated even analytically, let us consider V_{eff} for thin film geometries related to the thin film sample of Fig. 2 of the main text. Results are shown in Fig. **S2**, assuming that the entire thin film makes up the scintillation volume. The blue curve in Fig. **S2** corresponds to the sample considered in the main text (air - 500 nm Si - 1 μm SiO_2 - Si substrate), while the others differ by removal of the top Si layer (orange) and both Si layers (green). For simplicity, we show just the absorption of light coming at normal incidence (angles of incidence below 15° lead to very small changes in the absorption). Here, V_{eff} may be directly calculated by solving for the E and H fields induced by solving the Fresnel problem of a plane wave coming from the far field (as expected from reciprocity). The blue curve features somewhat well-defined and sharp resonant peaks corresponding to thin-film resonances associated with the guiding structure formed by silica surrounded by high-index silicon. Even in the case of silica surrounded by air, which in principle is the closest case to an intrinsic system, and provides minimal light-guiding, there is clear nanophotonic shaping that will arise from the etalon fringes: associated with the fact that the silica is a wavelength-scale thin-film. Thus, the observed scintillation spectrum would depart considerably from the singly-peaked Gaussian spectral function of the self-trapped hole (STH) defects in silica (which would represent the bulk spectrum).

Section C: Experimental setup

In this section, we describe our general experimental setup. It is based on a modified Scanning Electron Microscope (SEM) is shown in Fig. **S3**A. Let us outline a few other elements of the experimental setup. First, the purpose of Element 6 (flat mirror) is to send the optical signal to

the visible – near-infrared imaging and spectroscopy system, shown in the right side of Fig. **S3**A (Elements 7-15). Second, the polarization-insensitive beamsplitter (Element 8) sends part of the signal to a visible CCD Camera (Hamamatsu). The combination of Elements 4 (objective), 7 (tube lens), and 9 (camera) creates an image of the sample's surface, so the location of the electron beam interaction with the sample can be visualized. This facilitates the alignment of the experimental setup. Third, Elements 16-18 are used to scatter light off from the surface of the sample. Typically, an alignment mark (silver paste dot deposited on a unused sample location) is drawn on the sample surface, to align the imaging and spectroscopy functionalities of the setup. Fourth, a set of two lenses is used (Element 11) to focus the optical signal into the fiber input feeding the spectrometer (Elements 12-15). The spectrometer is comprised of a fiber coupling into a slit, a grating turret (Element 12), and a mirror focusing the signal on a visible CCD (Element 15).

SEM Control

The SEM beam current, voltage, working distance, and stage positioning are controlled in part with the Caesium Software provided by Applied Beams LLC (Oregon). Adjustment knobs outside the SEM chamber allow alignment of the emitter, focusing lenses, stage rotation and tilts.

Objective positioning

The XYZ positioning and tilt angle alignment of the objective (Element 4) is realized with a homemade motorized stage. The three motors are controlled through a computer interface outside the SEM chamber. Each motor is connected to an outside controller through a vacuum-preserving electronic connector.

Calibration measurement

The spectra measurements were converted to power spectral densities after performing a calibration measurement, whose setup is shown in Fig. **S3**B. The calibrated source (AVA Light - Element 19) of known power is positioned at the location of the objective / electron beam focus. The conversion relation is a linear mapping from the spectrometer signal to power spectral density:

$$S(\lambda) = P(\lambda)L(\lambda), \tag{9}$$

where $S(\lambda)$ is the spectrometer signal, measured in counts per second, $P(\lambda)$ is the signal spectral density measured in W/nm, and $L(\lambda)$ is a spectral loss function accounting for dispersive attenuation through the optical setup. $L(\lambda)$ is measured in (counts/s)/(W/nm). The reconstructed optical dispersive attenuation function $L(\lambda)$ is shown in Fig. **S3**C.

Additionally, we performed spectral calibration by measuring emission lines of a lamp with characteristic emission wavelengths (mercury lamp) and used three of those lines to calibrate the spectrometer. There may still be wavelength miscalibration between the lines used for calibration. We accounted for this possible mismatch in our fit with theory.

Section D: Additional experimental results

In this section, we provide additional experimental measurements. In a first series of experiments, we measure the polarization-dependence of the scintillation signal with a linear polarizer. As opposed to Smith-Purcell radiation (*17*), the recorded scintillation signal is polarization-insensitive (as opposed to polarized along the direction of electron beam propagation, as in the case with Smith-Purcell radiation). This observation is verified for both types of samples under study (photonic crystals and thin film).

Next, we measure the output spectra and ratio of green to red scintillation peaks with different angles of electron incidence. Results are shown in Fig. **S4**(c-d). As in the main text, we

examine the dependence of η_{rg}, ratio of green to red scintillation spectral peaks. We observe that the peak scintillation saturates at an angle below $\sim 5^\circ$ in both types of samples. This is accompanied by an increase of the red scintillation peak signal compared to the green scintillation peak signal (resulting in a decrease of η_{rg}).

Section E: Inverse-design of nanophotonic scintillator structures

In this section, we show how inverse-design techniques can be applied to optimize scintillation, enabling the discovery of scintillation structures that enable strong enhancements (up to 100-fold). To do inverse design effectively, we need an efficient method to compute V_{eff} and its gradient, and to this end, we make use of rigorous coupled wave analysis (RCWA) (*67*).

RCWA is used to calculate $V_{\text{eff}}^{(i)}(\omega, \Omega)$ and its gradient with respect to continuous degrees of freedom describing the scintillator's geometry. In both cases, the patterned layer's permittivity is decomposed into a square lattice of pixels, whose value can be continuously tuned between 0 (corresponding to fully-etched, air or vacuum permittivity) and 1 (silicon). The gradients of the objective function are obtained via automatic differentiation (in our case, using Python autograd) (*68*).

Our numerical methods calculate the $V_{\text{eff}}(\omega)$ at normal incidence and its gradient with respect to the degrees of freedom ϵ_i (via automatic differentiation) – therefore we drop the angular dependence in V_{eff} in this section. By plugging the forward and gradient calculations into a non-linear optimizer (MMA from NLOpt (*69*)), topology optimization can discover local optima of a differentiable cost function. In the examples from this section, we consider the following constrained optimization problem:

$$\begin{cases} \max_{\epsilon_i} V_{\text{eff}}(\omega|\epsilon_i) = \int_{V_{\text{SiO}_2}} d\mathbf{r} \frac{|E(\omega,\mathbf{r}|\epsilon_i)|^2}{|E_{\text{inc}}(\omega)|^2} \\ \text{s.t. } 0 \leq \epsilon_i \leq 1, \forall i, \end{cases} \tag{10}$$

where $E(\omega, \mathbf{r}|\epsilon_i)$ is the induced field at position $\mathbf{r}$ by normally-incident plane wave field $E_{\text{inc}}(\omega)$ in a structure defined by degrees of freedom ϵ_i. Since we are considering normal emission only,

we dropped the angular and polarization dependence in the definition of V_{eff}. ω is chosen to be the frequency of interest for the optimizer (the center frequency of the scintillation defect, $\lambda =$ 670 nm or 477 nm for the red and green peaks, respectively). When optimizing over the entire defect bandwidth, the optimization problem is rephrased as:

$$\begin{cases} \max_{\epsilon_i} \sum_j \alpha_j V_{\text{eff}}(\omega_j|\epsilon_i) \\ \text{s.t. } 0 \leq \epsilon_i \leq 1, \forall i, \end{cases} \tag{11}$$

where ω_j is a set of frequencies of interest and α_j a weight corresponding to the frequency's weight in the scintillation spectrum (typically, a Gaussian around the center scintillation frequency). With this definition, we are implicitly assuming that the HEP energy loss density is uniform in the scintillating volume.

In Fig. **S5**(a-c) we present results obtained by maximizing $V_{\text{eff}}^{(i)}(\omega, \Omega)$ via topology optimization. The parameters for the design shown in Fig. **S5**(a-b) are the following: silicon (thickness 500 nm: etched 50 nm + uniform 450 nm) - silica (thickness 300 nm) - silicon (substrate). The photonic crystal has periodicity 430 nm. The simulation enforces C_{4v} symmetry of the degrees of freedom, which are discretized on a 50 $\times$ 50 square unit cell. Density and binarization filters are gradually applied to increase the minimum feature size to $\sim$ 5 pixels (43 nm).

The parameters for the designs shown in Fig. **S5**C are the following: silicon (thickness 500 nm: etched 50 nm + uniform 450 nm) - silica (thickness 20 nm) - aluminium (substrate). The photonic crystal has periodicity 430 nm. The simulation enforces mirror symmetry of the degrees of freedom, which are discretized on a 100 pixel (one-dimensional) unit cell. Density and binarization filters are gradually applied to increase the minimum feature size to $\sim$ 3.5 pixels (15.5 nm). For all designs, RCWA convergence with respect to the number of Fourier order coefficients was verified. After discovery of an optimized design with RCWA-based topology optimization, we calculate the final V_{eff} with a commercial finite-difference time-domain solver (Lumerical FDTD).

The spectra obtained with FDTD of the designs discovered with our RCWA-based topology-optimization algorithm are presented in Fig. **S5**. Peak enhancement of $\times 11$ is obtained compared to an unpatterned structure (silicon - silica - silicon) with the two-dimensional pattern shown in Fig. **S5**A. Meanwhile, $\times 5$ enhancement is found compared to the "bare" structure (silica - silicon). Additionally, the one-dimensional patterns (grating-like structures) shown in Fig. **S5** achieve peak enhancements of (compared to unpatterned samples): $\times 86$ for the green scintillation peak (single frequency), $\times 78$ for the red scintillation peak (single frequency), and $\times 30$ for the red scintillation peak (bandwidth optimization).

In future works, we will consider integrating our inverse-design method into an end-to-end scintillation pipeline for specific applications, also considering the HEP energy loss spatial distribution and image reconstruction algorithms (from the detected scintillation signal). Such end-to-end frameworks have recently been proposed in the context of nanophotonic imaging. This may be particularly interesting for high-resolution x-ray imaging, where optimal resolutions are pursued with constraints on HEP dose, and scintillator thickness.

Section F: UV Scintillation shaping in hexagonal boron nitride

In this section, we extend the scope of the general nanophotonic theory of scintillation developed in Section B. In particular, we show how our framework can be used to design highly efficient scintillation sources in the UV. Additionally, we show that our framework can describe how the scintillation spectrum is altered by the presence of gain, enabling for the first time a framework to describe amplification effects in scintillation, potentially enabling description of interesting experimental results such as scintillation-lasing in Watanabe et al. (*70*). The perspective of tunable ultraviolet sources is especially exciting given the growing interest in ultraviolet sources for water purification and sanitization. In particular, several wavelengths in the UV-C window have been of interest (*71*), with some gaining renewed interest in the far-UVC to

eliminate airborne human coronaviruses (*72*).

In this section, we focus primarily on UV scintillation from hBN (hexagonal boron nitride), where Watanabe *et al.* demonstrated efficient UV emission from high-quality hBN substrates pumped by electron beams.

First, let us consider scintillation from a simple thin-film of hBN. For concreteness, we consider an isolated film of BN of thickness 1 μm surrounded by air (mimicking the isolated BN flakes in Watanabe *et al.* (*70*). Then we consider the emission per unit area (which is independent of lateral position along the film) for a beam normally incident on it. To calculate the spectrum, we must multiply the intrinsic luminescent spectrum of BN with V_{eff}, which can be readily calculated (by solving for the fields inside the BN resulting from an a plane wave impinging on the air-BN-air system). For the purposes of this section, we are mostly interested in the relative magnitude of the signal between different sample conditions, and not as interested here in the absolute magnitude of the luminescence spectrum, which requires a detailed microscopic understanding of the excitons contributing to the BN signal. Thus, the intrinsic scintillation spectrum for the planar system is taken phenomenologically as the function shown in Fig. **S6**(inset), with peak intensity at 216 nm and a width of roughly 5 nm. This function is taken to be in qualitative agreement with the spectrum measured in Ref. (*70*). To showcase the kinds of predictions that can be made the formalism of Sec. B, we show the predicted luminescence of hBN as the intrinsic losses of the BN permittivity are reduced. This is to simulate the effect of gain induced by electron beam pumping. As the loss is reduced, the luminescence spectrum starts to manifest growing and narrowing etalon peaks. This feature is in accord with observations in Ref. (*70*), which show spectral narrowing and strongly increased intensity as a function of electron-beam pumping of hBN flakes.

Next, we demonstrate control and enhancement of hBN ultraviolet scintillation with nanopatterned structures, shown in Fig. **S7**. The structures that are used are shown in Fig. **S7**A: a two-

dimensional square periodic array of holes etched in hBN (thickness 100 nm) on top of a silica spacer (thickness 200 nm) on top of an aluminium substrate. The period of the structure equates to 180 nm. We compare emission power spectra at various radii (unpatterned structure, $r = 30$ and $r = 50$ nm) and beam locations (shown schematically in Fig. **S7**(a,c)).

We assumed that the hBN layer consists of deformed monocrystalline samples similar to the ones in Ref (*70, 73*). Such samples, not unlike polycrystalline hBN, exhibit a greater number and variety of scintillating defects. We used for our theory an empirical fit of the spectrum shown in Fig. 6 (blue line) of (*73*).

The resulting spectra are shown in Fig. **S7**(d,e). The peak emission wavelength can be tuned by adjusting the radius and the relative and absolute power of the observed peaks can be controlled by exciting the structures at different locations (which can be realized by operating state-of-the-art SEMs with < 5 nm spatial resolution and beam size in spot mode).

Section G: Additional Density Functional Theory (DFT) Calculations

In this section, we present additional density functional theory (DFT) calculations pertaining to the electronic structure of the STH defects responsible for scintillation in silica. We also provide more technical details regarding the DFT calculations used in the main text, expanding upon the discussion in the Methods section.

DFT calculations were implemented through JDFTx (*61*) using norm conserving pseudopotentials (*74*). Calculations were performed on either molecular clusters or bulk models of α-quartz. The luminescent defects in our study are polarons (*75*) – excess charge carriers that localize by perturbing the ionic lattice through the electron-phonon interaction. Polarons are known to be difficult to model through standard DFT techniques (*76*). This is because standard DFT functionals, such as the widely used gga-PBE, are often inadequate in describing materials in which there are strong self-interaction effects.

We overcome the challenges posed by the self-interaction effect through a multifaceted approach: first, we model clusters with the Boese-Martin hybrid functional (*63, 77*), which includes 42% exact exchange. This mixing of Hartree exchange compensates for the inadequacy of standard DFT functionals in accounting for self-interaction effects (*76*) . We also use Coulomb truncation to avoid interactions between adjacent clusters, as is necessary in a plane wave basis (*64*). We find that this produces a model with absorption peaks that are in agreement with our experimental results and the literature (*75, 78–81*). Second, we also use a bulk model for α-quartz. In this case, in order to form a polaron, we impose a constraint that each unit cell of our model must have a 1 Bohr magnetic moment. This constraint enforces the localization of the spin density. Note that without this constraint, the addition of a hole in each unit cell would not cause an overall spin polarization, as this would just correspond to depleting the top most valence band by half of its electrons. It is this constraint on the magnetization of the system that enforces a polaron to form. Bulk calculations of our defect were implemented with standard gga-PBE exchange correlation (*65*). The motivation for this is that the magnetization constraint enforces localization and thus mimics the self-interaction effects that are neglected by the gga-PBE functional.

Bulk models

We summarize the results presented in the main text. First, let us consider a bulk model of α-quartz with a $6 \times 6 \times 6$ k-point sampling and a 25 Hartree wavefunction cutoff. The oscillator strength spectrum is shown in Fig. **S8**. This was computed both with dipole and momentum matrix elements. In the dipole case, we get spectral peaks at 645 and 481 nm and in the momentum case, we get peaks at 650 and 473 nm. Either case is compatible with the experimental results and the literature.

In the case of the bulk defect, we get a well-localized polaron bridging two oxygen atoms.

The spin density (shown in Fig. 3B of the main text) derived from our bulk calculations is consistent with what has been previously reported as the STH2 defect in silica. The spin densities on the two oxygen atoms are found to be 0.473 and 0.399 Bohr. All other atoms in the unit cell have negligible spin densities.

To further examine the consistency of our proposed defect model with previous findings on STH2, we analyze the hyperfine coupling constants as implemented through gauge including projector augmented waves (GIPAW) (*82*). We find some asymmetry between the two bridging oxygen atoms, indicating that our model is not "pure STH2". For the oxygen with a higher share of the spin density, we find a Fermi contact interaction of -2.7 mT. While for the lower spin density oxygen we find a Fermi contact interaction of -2 mT. Note that the ratio of these two numbers must be exactly the ratio of the spin densities at the oxygen centers since the Fermi interaction is the isotropic contribution to the hyperfine tensor. For the higher spin density oxygen, we get (in the basis of principal axes) hyperfine couplings: -1.1, -1, -6.1. For the second oxygen atom, we obtain couplings: -0.57, -0.5, -4.9. These values are also consistent with reported values in the literature (*80*).

Finally, we propose another model for STH1, the polaron defect attributed to a highly localized spin density on a single oxygen has previously been described using cluster models. Here we produce a bulk model, again using a magnetization constraint of 1 Bohr/unit cell. For this bulk model, however, we do not perturb any atoms from their relaxed positions and we use exact Hartree-Fock exchange to enforce the localization of the defect. The calculated spin density is shown in Fig. **S9**.

We note that in the case of STH1, exact exchange together with the aforementioned magnetization constraint is required to obtain correct localization. This may be attributed to the fact that the symmetry of the system does not allow for an asymmetric spin density unless exact exchange is used.

Cluster models

We analyzed several manifestations of possible polaron geometries in cluster formations. We devised a minimal model for STH using 2 oxygen atoms and passivating hydrogens. The results for a few cluster geometries are given in Fig. **S10**, Fig. **S11**, and Fig. **S12**, labeled 1, 2, and 3, respectively. In particular, cluster 1 shows a plausible spin density as shown in Fig. **S10**A.

Alternative DFT and rate equation models

In a last model, we calculate energy levels and spectra of a cluster model without hybrid functionals. DFT calculations were performed using norm-conserving (SG-15) pseudopotentials, a 30 Hartree plane wave cutoff, and the gga-PBE exchange correlation functional in a 21 atoms cluster to model the STH defect. The Si-O-Si bonding angle is changed to create a distribution of possible manifestations of the defect, and the excitation spectra and oscillator strengths are obtained through momentum matrix elements.

Based on this DFT model, a simplified four-level system is designed to model electron pumping and subsequent radiative emission from defect states in silica. The model is pictured in Fig. **S13**B, corresponding to calculated energy levels from the DFT model in Fig. **S13**(a, bottom). The following rate equations are used to model the system:

$$\begin{cases} \frac{dp_1}{dt} = & -\Gamma_{41}\, p_1(1-p_4) + \Gamma_{12}\, p_2(1-p_1) + \Gamma_{13}\, p_3(1-p_1) \\ \frac{dp_2}{dt} = & \Gamma_{24}\, p_4(1-p_2) - \Gamma_{12}\, p_2(1-p_1) \\ \frac{dp_3}{dt} = & \Gamma_{34}\, p_4(1-p_3) - \Gamma_{13}\, p_3(1-p_1) \\ \frac{dp_4}{dt} = & \Gamma_{41}\, p_1(1-p_4) - \Gamma_{24}\, p_4(1-p_2) - \Gamma_{34}\, p_4(1-p_3) \end{cases} \tag{12}$$

such that the total occupation probability is conserved over time $\frac{d\sum_i p_i}{dt} = 0$ with the initial condition $p_1 = 1$ and $p_{i\neq 1} = 0$. This set of equations describes a four-level system, where 1 is the ground state, 4 is a high-energy state to which electrons are sent via free-electron pumping (since the free-electron energy is much larger than any other energy scale in the bandstructure).

Band electrons can relax from the higher-energy state 4 to one of two intermediate states 2 and 3, corresponding to the red and green defect states, respectively.

Since excitation and relaxation mechanisms happen on a much shorter timescale than emission for most scintillating systems, we can assume that $\Gamma_{34}, \Gamma_{24} \gg \Gamma_{13}, \Gamma_{12}$. We can solve the steady-state of Eq. 12 to estimate the ratio of green to red emission at the steady-state:

$$\eta = \frac{\Gamma_{13}\, p_3}{\Gamma_{12}\, p_2}. \tag{13}$$

We use this model to gain further microscopic understanding of the observed experimental data, in conjunction with the general nanophotonic scintillator theory described in the main text. We chose η as an experimental observable, since it can be calculated from Eq. 12 and – assuming green and red peak defects are localized in the same region – the observable is independent of a few experimental unknowns (beam size, number of excited emitters). Electrons in states 2 and 3 can then radiatively decay into state 1.

In a first numerical experiment shown in Fig. **S13**(d, left), we utilized scintillation data measured on the TF sample at various incident voltages and currents. This data was used to estimate the ratio of decay rates $\Gamma_{34}/\Gamma_{24} = 2.45 \pm 0.7$.

We assume that Γ_{41} is proportional to the electron beam energy deposited in the luminescent material: $\Gamma_{41} \propto I \times E \times \eta_{\text{ene}}(E)$ where I is the incident electron current, E its kinetic energy (in keV), and $\eta_{\text{ene}}(E)$ the fraction of energy (normalized to the incident energy E) deposited by an electron in the silica layer, calculated via Monte Carlo simulations of electron energy loss in the TF sample.

In a second numerical experiment shown in Fig. **S13**(d, right), we utilized scintillation data measured on the PhC sample at various incident voltages and currents. This data was used to estimate the ratio of decay rates enhancements Γ_{13}/Γ_{12} and to confirm the value of Γ_{34}/Γ_{24}. When letting both parameters be optimized, we obtain a value of $\Gamma_{34}/\Gamma_{24} = 2.37 \pm 1.4$, close

to the original value. We can also estimate the value of $\left(\frac{\Gamma_{12}}{\Gamma_{13}}\right)_{\text{PhC}}\left(\frac{\Gamma_{12}}{\Gamma_{13}}\right)_{\text{thin}}^{-1} \sim 3.56$ which corresponds to the V_{eff} scintillation enhancement. Therefore, results from the four-level model are a strong indication of the microscopic nature of the observe scintillation spectrum.

We verified the robustness of our fits by trying different values of the ratio Γ_{12}/Γ_{24}, different differential equation solvers, and did not observe any significant change in the values obtained for the parameters of interest, which indicates the consistency of our approach.

Section H: Additional x-ray scintillation data

In this section we provide additional measurements and characterizations of the x-ray scintillation experiment.

FIB etching of photonic crystals in YAG:Ce crystals

First, we detail the fabrication of nanoscale patterns at the surface of a YAG:Ce (Cerium-doped yttrium aluminum garnet) substrate. The substrates were acquired from Crytur (Czech Republic). They were grown using a modified Czochralski method and processed to thin flat surface plates.

We acquired several YAG:Ce samples (20, 50, and 100 μm thick) and used a VELION FIB-SEM to pattern the photonic crystal. The FIB-SEM tool used here is dedicated to large-area nanofabrication and rapid prototyping. VELION FIB-SEM comprises a top down mounted nanoFIB column perpendicular to a Laser Interferometer Stage with an attached SEM column. The instrument is highly optimized for fabricating high resolution, 2D and 3D nanostructures. Before patterning, a thin layer of Au (5-15 nm) is deposited to prevent charging issues. After patterning, the layer is removed in a bath of Au selective etchant.

We used several FIB doses in these experiments:

1. Dose A: Au^+ ions in a 40 μm aperture, 1 nC/μm^2.

2. Dose B: Au^+ ions in a 20 μm aperture, 0.3 nC/μm^2 with a design diameter of 100 nm.

3. Dose C: Au^+ ions in a 30 μm aperture, 1 nC/μm^2.

Influence of filters

The experiment was carried out with the experimental setup shown in the main text (Fig. 4). We present additional measurements here to corroborate the claims presented in the main text.

We record the scintillation spectrum from the entire scintillator plate with a fiber-coupled OceanOptics spectrometer USB2000. The results are shown in Fig. **S14**, which is consistent with the literature and with characterization provided by the sample provider. On the same plot, we show the range of several filters that were used in this experiment. In x-ray imaging experiments shown in Fig. 5 of the main text, the source-to-specimen and specimen-to-scintillator distances are both $\sim$ 1 cm, which results in a geometric magnification of $\sim$ 2.

We recorded the scintillation from the patterned PhC area using various optical filters (see Fig. **S14**) and various x-ray filters (whose name takes the form LEX or HEY, where "LE" (resp. "HE") stands for low-energy (resp. high-energy) and X, Y are numbers. The x-ray filters are positioned right after the x-ray source, and the location of the optical filters in the setup is shown in Fig. 4 of the main text. The x-ray spectrum, provided by the microCT scanner manufacturer (Zeiss), exhibits a broad background (5-100 keV) with a few narrow peaks at well-defined x-ray frequencies (namely 10, 58, and 68 keV). In addition to the data provided in the main text, we show the x-ray scintillation signal measured for the same sample for various sets of visible and x-ray filters. Visible filters are used to remove background from the glass objective scintillation. The measured enhancement is consistently in the range 2.68-2.7 using visible filters FF01-549-15-25 (narrow bandwidth 549 ± 15 nm). It decreases to 2.4-2.6 for broad bandwidth filters, possibly because of the larger scintillation background.

RCWA modeling and influence of geometrical parameters and optical loss

To determine the influence of geometrical parameters and optical loss on the scintillation enhancement, we measured the scintillation enhancement from multiple samples from various wafers, with varying thicknesses, hole diameters and depths, patterned areas, and FIB doses (A, B, or C). Our compiled results are shown in Table **S1**. For each sample, we measured the hole diameter and depths after Au removal with atomic force microscopy (AFM). These data were used in our simulations. All AFM cuts in Fig. **S16** can be fitted to a $\sin^2$ function with period 430 nm, corresponding to the design period. We observed deviations from the fit because of variations in depth, radius, and period. The estimated error on the depth is of ± 10nm by comparing depths across samples and across lines within one sample. Therefore, the permittivity profile used in our RCWA simulations is of the form $\epsilon(x,y) \propto \sin^2(xL/\pi)\sin^2(yL/\pi)$ where $L = 430$nm, interpolating between the permittivity of YAG:Ce and that of vacuum. We also calculated RCWA absorption profiles for periodic array of holes with flat sidewalls and obtained similar results. One such example of RCWA calculations is shown in the main text (Fig. 4). We perform a similar comparison between our theory and experiments in Fig. **S17**. A typical raw spectrum of a patterned scintillator is shown in Fig. **S17**A: the sharp spectral peaks originate from multiple resonant channels coupling in a thick scintillator (whose thickness is much larger than the wavelength). Additional theory and corresponding experiment are shown in Fig. **S17**, respectively. In Fig. **S17**, the predicted enhancement is shown for various depths (24, 34, and 44 nm), corresponding to the mean $\pm$ error bar of the measured depth with AFM (reported in Fig. **S16**). The calculated enhancement is of 5.1 ± 3.0. Though the measured enhancement of 2.3 is below the predicted one with shallower etch depth, additional uncertainties on the hole radius, periodicity, or material optical absorption can explain the measured enhancement. Specifically, we observe that by increasing optical losses in YAG from $\mathrm{Im}(\epsilon) = 10^{-6}$ (corresponding to the value given by the wafer supplier) to $\mathrm{Im}(\epsilon) = 10^{-5}$, all of the predicted enhancements can be

fitted to the measured ones.

The scintillation enhancement at constant x-ray exposure (dose) directly translates into faster scans to achieve a given brightness. The scaling of the brightness versus scan integration time is shown in Fig. **S18**, measured on sample A1 (100 μm). We observed that the scan time to achieve a given brightness was reduced by the same enhancement factor when comparing the bare and PhC samples.

We also observed that adding a silver reflector on the back face of a scintillator increased the scintillation signal by a factor of ~ 2. To confirm this prediction, we measured an experimental enhancement of 1.9, when comparing an unpatterned scintillator with and without a back-reflector. The back-reflector consisted of a silver thin film with thickness 150 nm deposited at the back-surface of a 20 μm-thick YAG:Ce scintillator.

Flat-field corrections

The VELION FIB-SEM used for nanofabrication is optimized for large-scale patterning with very high-precision and low stitching errors. Still, given the high currents and large aperture we are using, the edges of the beam at the edge of the writing field is slightly asymmetric, which results in dose variations at the edges of the writing field. The edges of the stitched writing fields are therefore apparent in x-ray images. We show in Fig. **S19** that flat-field correction can be used to eliminate those artifacts. More specifically, we record a flat-field image of the scintillator illuminated by an x-ray source without any specimen in the way, and divide the original image by the flat-field image.

Supplementary Figures

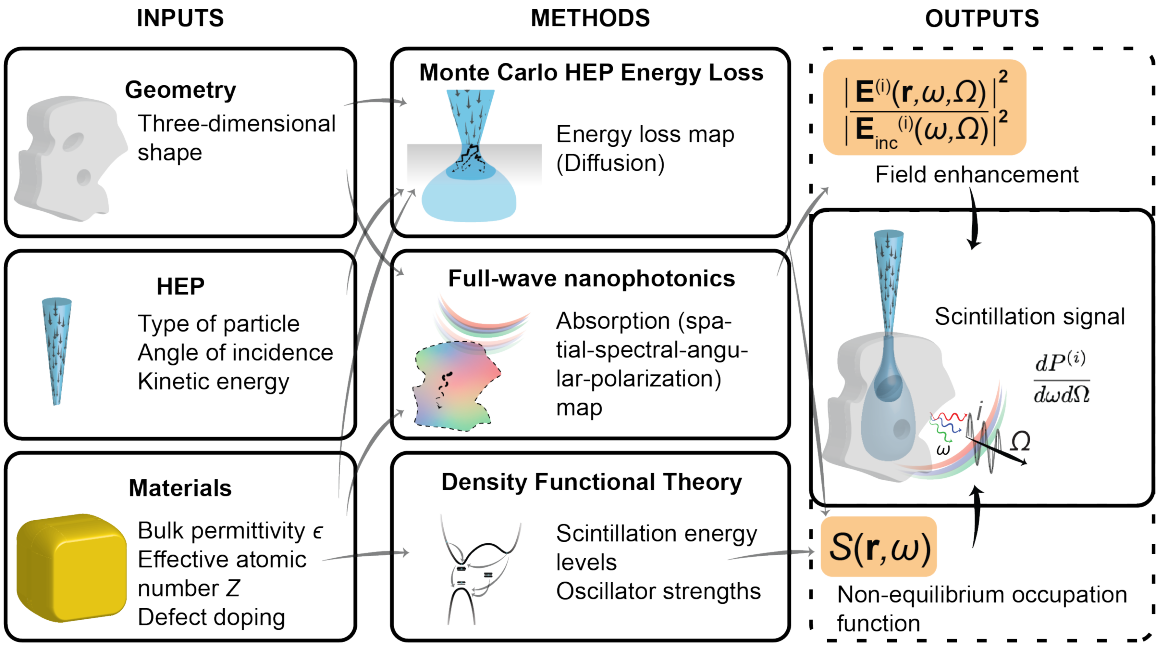

Fig. S1: **End-to-end scintillation framework.** Arrows represent forward flow of information from inputs to outputs through our simulation methods (as an example: geometry information feeds into energy loss calculations, which provides an energy loss map that feeds into the spectral function). HEP: high-energy particle. $dP^{(i)}/d\omega d\Omega$: scintillation spectral-angular power density at polarization i. ω: scintillation frequency, Ω: scintillation angle of emission. $S(\mathbf{r},\omega)$: non-equilibrium steady-state distribution function. $\left|\mathbf{E}^{(i)}(\mathbf{r},\omega,\Omega)\right|^2 / \left|\mathbf{E}_{\text{inc}}^{(i)}(\omega,\Omega)\right|^2$: field enhancement at location $\mathbf{r}$, frequency ω, angle Ω.

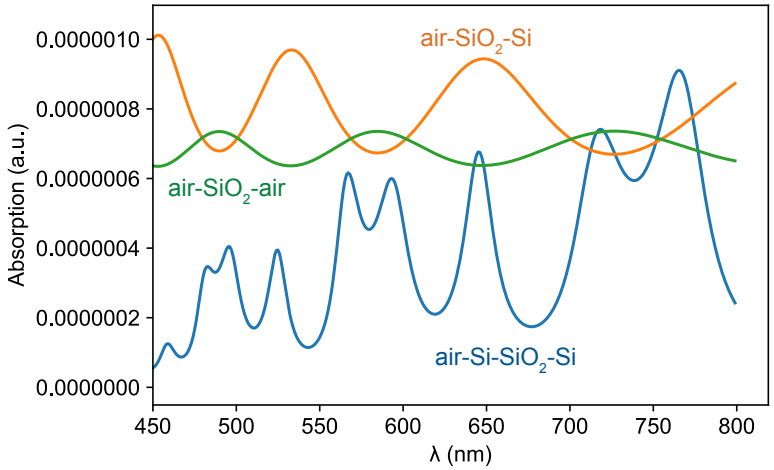

Fig. S2: **Absorbed power (proportional to $V_{\mathbf{eff}}$) at normal incidence as a function of wavelength for a few different thin film geometries.** Thicknesses for blue curve: $\infty - 500$ nm $- 1000$ nm $- 500$ nm $- \infty$. Thicknesses for orange curve: $\infty - 1000$ nm $- \infty$. Thicknesses for green curve: $\infty - 1000$ nm $- \infty$.

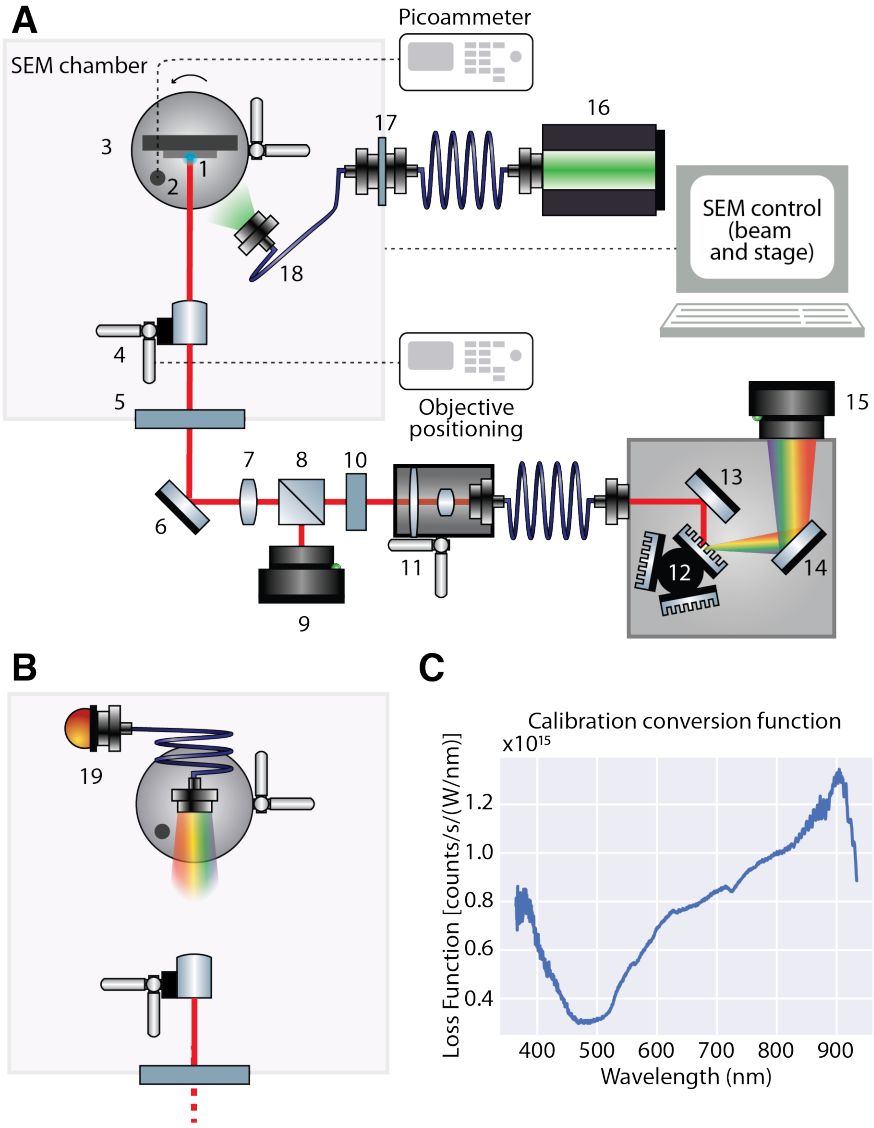

Fig. S3: **Schematic of the experimental setup and calibration measurement.** (**A**) Schematic of the experimental setup. Inside SEM chamber: 1: Electron beam interacting with sample; 2: Faraday cup, connected to external picoammeter, measuring incident current. 3: 6-axis, fully eucentric stage, controlled by SEM control. 4: XYZ objective stage. 5: x-ray blocking window. Outside SEM chamber: 6: Mirror. 7: Tube lens. 8: Beam splitter. 9: CCD Camera, imaging sample surface. 10: polarizer (optional). 11: XYZ cage assembly with two focusing lenses and a fiber-coupling. Inside spectrometer: 12: Grating turret. 13, 14: (Focusing) Mirrors. 15: Spectrometer CCD. Green laser feedthrough alignment arm: 16: Green laser source. 17: Fiber-coupling feedthrough, vacuum compatible. 18: Fiber output illuminating sample. (**B**) Calibration experiment (the rest of the setup is not shown because it is similar to (**A**)). 19: AVA Calibration light source. (**C**) Measured calibration conversion function.

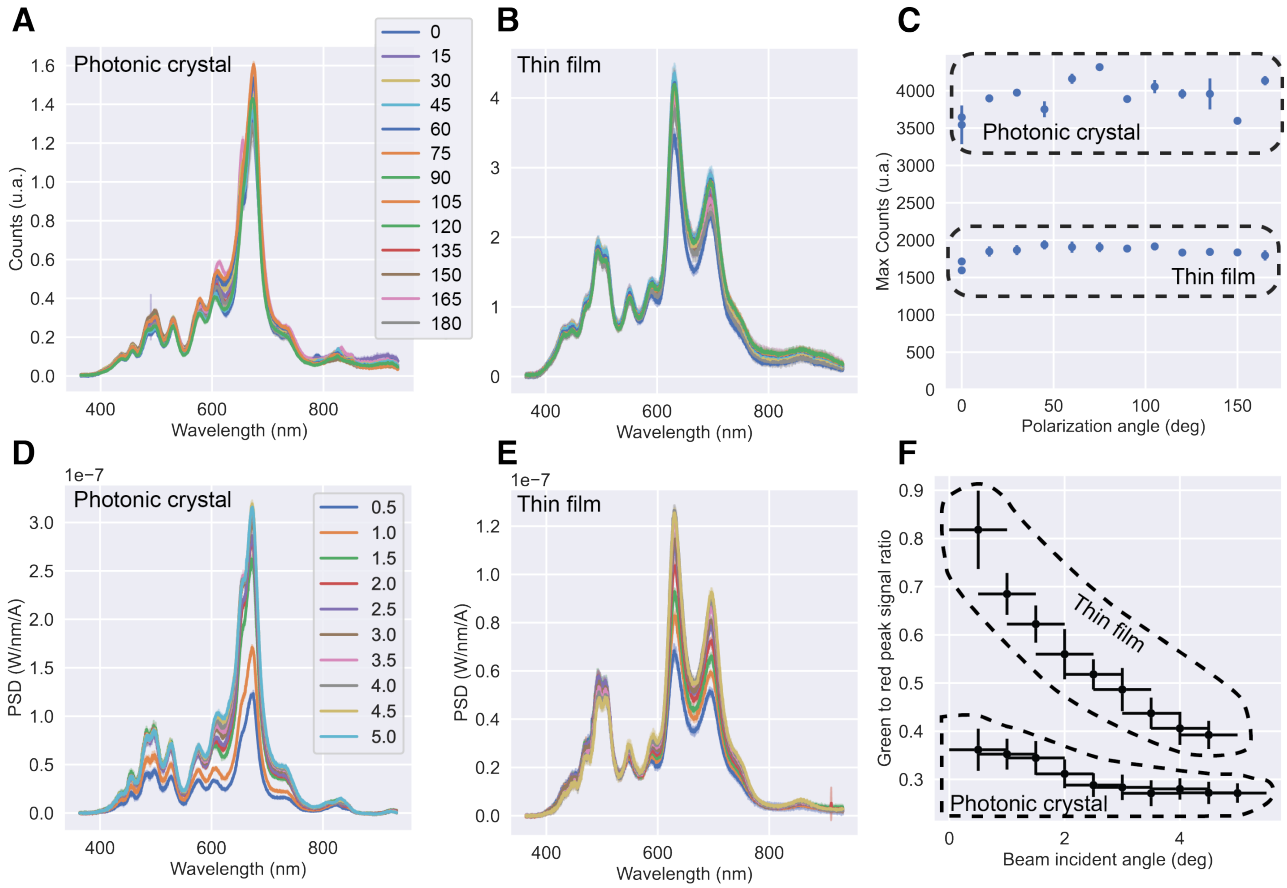

Fig. S4: **Additional experimental data: polarization-dependence and influence of HEP incidence angle.** (**A**) Scintillation spectra as a function of polarization angle (photonic crystal). (**B**) Scintillation spectra as a function of polarization angle (thin film). (**C**) Maximum of scintillation spectrum as a function of polarization angle (photonic crystal and thin film samples). (**D**) Scintillation spectra for various HEP incidence angles (photonic crystal). (**E**) Scintillation spectra for various HEP incidence angles (thin film). (**F**) Green to red peak ratio as a function of the HEP incident angle (photonic crystal and thin film).

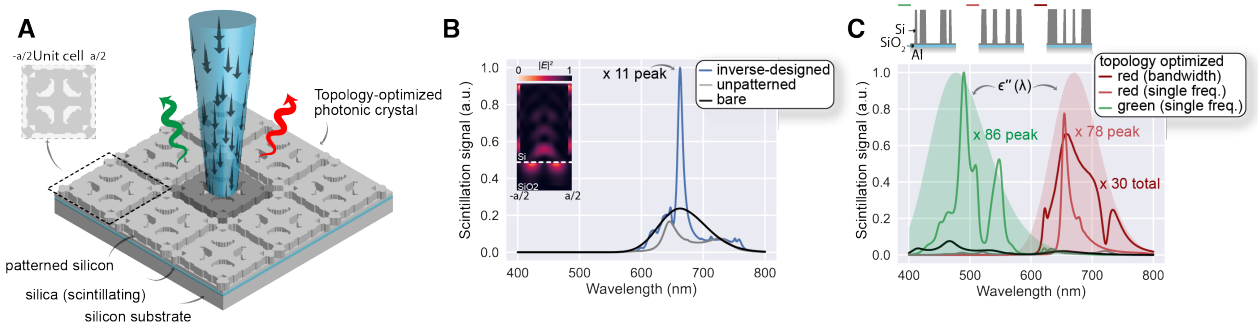

Fig. S5: **Optimized nanophotonic scintillators.** (**A**) Topology optimization can be leveraged to discover optimized nanophotonic scintillators, here embodied in a patterned silicon-on-insulator wafer under electron-beam excitation. (**B**) The optimized design can find local optima of V_{eff} which then translate into increased scintillation yields. (**C**) Similar optimized nanophotonic scintillators can be discovered for two-dimensional designs (silicon on silica and metallic substrate). The optimized nanophotonic scintillators optimize the scintillation yield of the red defect (integrated over bandwidth), red (just over its center frequency), and green (center frequency) scintillating defects, respectively.

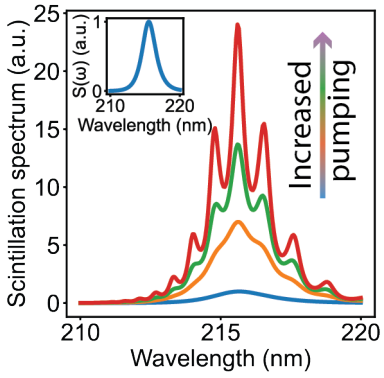

Fig. S6: **Amplified hBN scintillation in hBN flakes.** Inset: Phenomenological intrinsic scintillation spectrum. Parameters used in this plots were chosen in accordance with (*70*). As a function of increased pumping, the losses are reduced (as the system moves towards transparency), leading to the spectrum manifesting growing and narrowing etalon peaks associated with thin-film resonances.

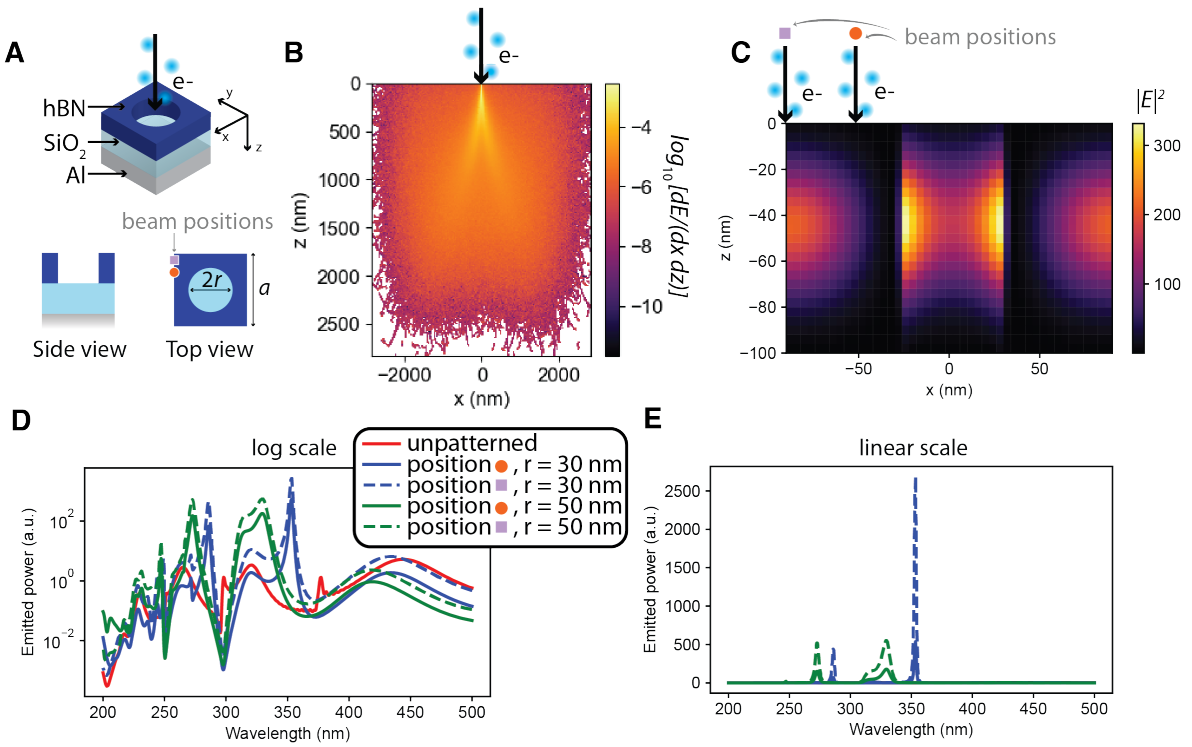

Fig. S7: **Tunable ultraviolet nanophotonic scintillators.** (**A**) Schematic of the design: etched hBN on a silica spacer on an aluminium substrate. (**B**) Marginal (integrated over y) energy loss probability distribution (log scale). (**C**) Total in-plane electric field distribution ($|E_x|^2 + |E_y|^2$) at $\lambda = 350$ nm). Our theory predicts the emitted scintillation power at various locations and etch radii, shown in log (**D**) and linear (**E**) scales.

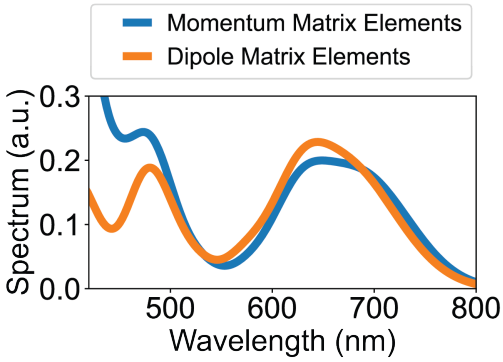

Fig. S8: **Calculated spectrum of the polaron defect from a bulk density functional theory (DFT) model of α-quartz.**

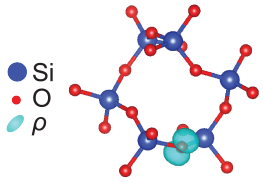

Fig. S9: **Spin density of STH1 calculated using a DFT model with exact Hartree-Fock exchange.** Si: silicon, O: oxygen, ρ: spin-polarized density.

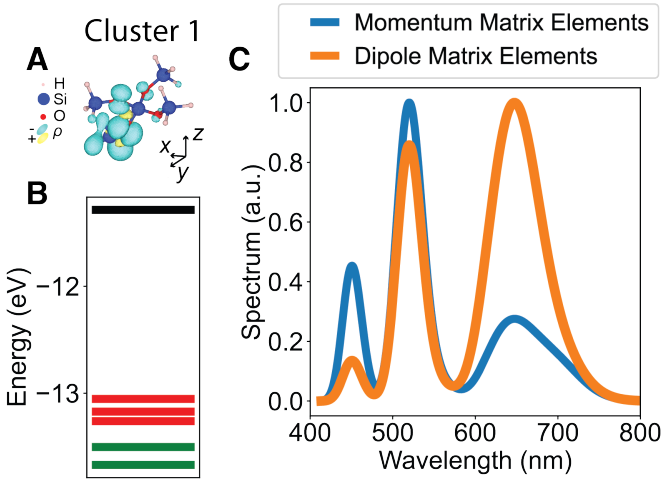

Fig. S10: **DFT calculation results for cluster 1.** (**A**) Spin density. H: passivating hydrogen, Si: silicon, O: oxygen, ρ: spin-polarized density, blue (negative), yellow (positive). Total spin density shared between the two bridging oxygen atoms is 0.78. (**B**) Defect energy levels. Green: green scintillation peak ground state, red: red scintillation peak ground state, black: excited state. (**C**) Spectrum.

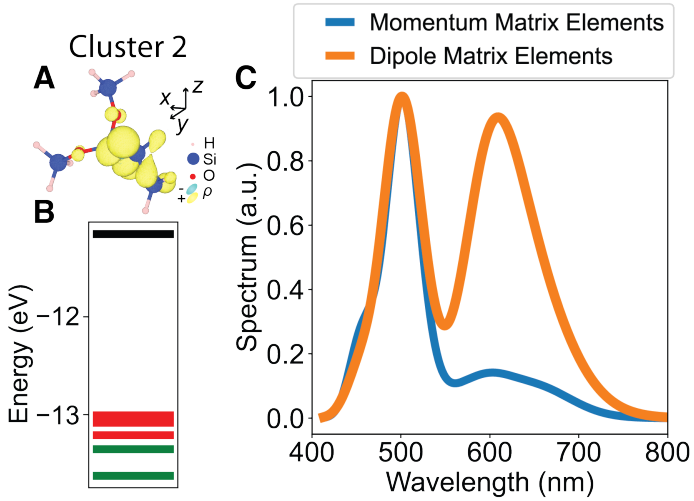

Fig. S11: **DFT calculation results for cluster 2.** (**A**) Spin density. H: passivating hydrogen, Si: silicon, O: oxygen, ρ: spin-polarized density, blue (negative), yellow (positive). Total spin density shared between the two bridging oxygen atoms is 0.8. (**B**) Defect energy levels. Green: green scintillation peak ground state, red: red scintillation peak ground state, black: excited state. (**C**) Spectrum.

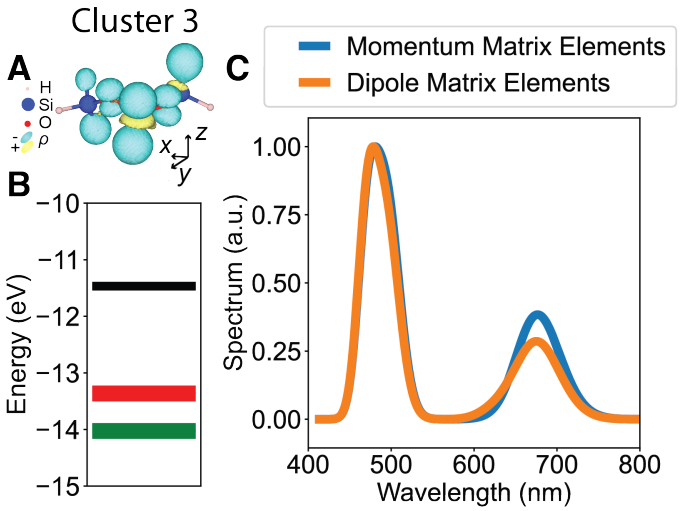

Fig. S12: **DFT calculation results for cluster 3.** (**A**) Spin density. H: passivating hydrogen, Si: silicon, O: oxygen, ρ: spin-polarized density, blue (negative), yellow (positive). The total spin density shared between the two bridging oxygen atoms is 0.36. (**B**) Defect energy levels. Green: green scintillation peak ground state, red: red scintillation peak ground state, black: excited state. (**C**) Spectrum.

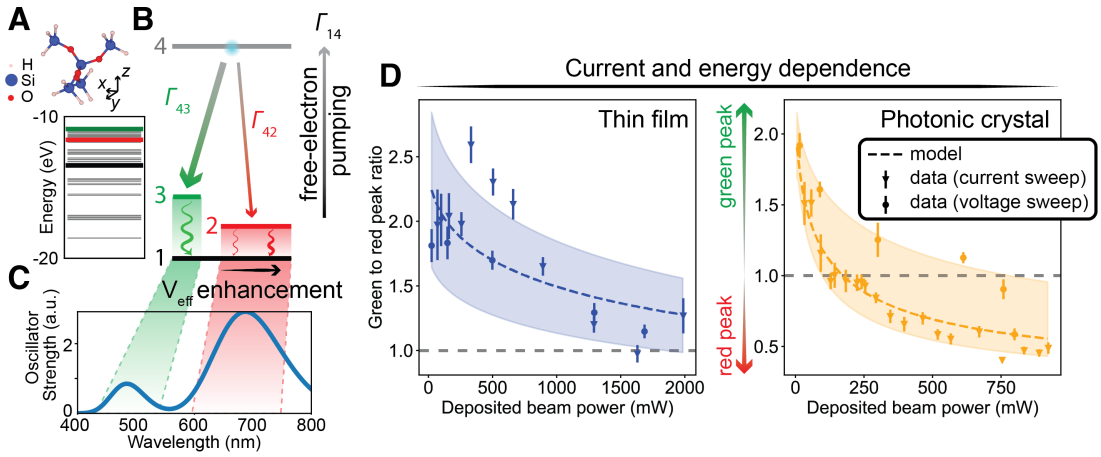

Fig. S13: **Alternative DFT and rate equation models for STH in silica.** (**A**) Top: 3D molecular model of STH defect in silica. Bottom: Calculated STH defect energy levels via DFT without hybrid functionals. (**B**) Simplified four-level system modelling the microscopics of electron scintillation in silica. (**C**) Calculated oscillator strength spectrum. (**D**) TF (left) and PhC (right) scintillation peak ratios as a function of deposited beam powers through electron pumping. The dashed line corresponds to the mean model prediction and the shaded area to the prediction from the model parameters $\pm$ their standard deviation (TF: uncertainty on Γ_{34}/Γ_{24}; PhC: uncertainty on Γ_{12}/Γ_{13}.

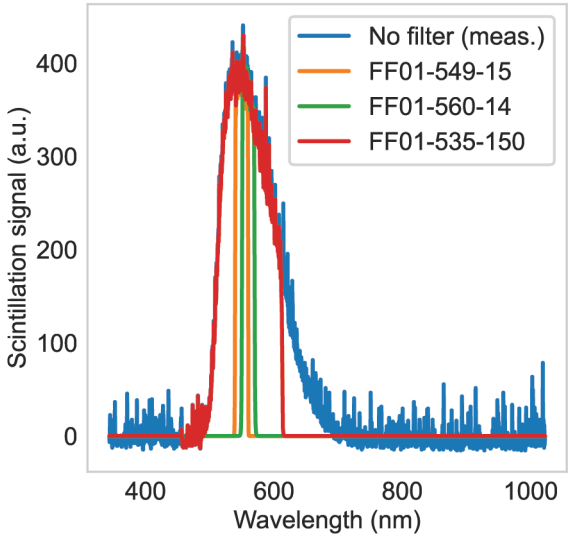

Fig. S14: **Measured x-ray scintillation spectrum from YAG:Ce scintillator (blue)**. The effect of several filters is calculated based on data provided by the manufacturer.

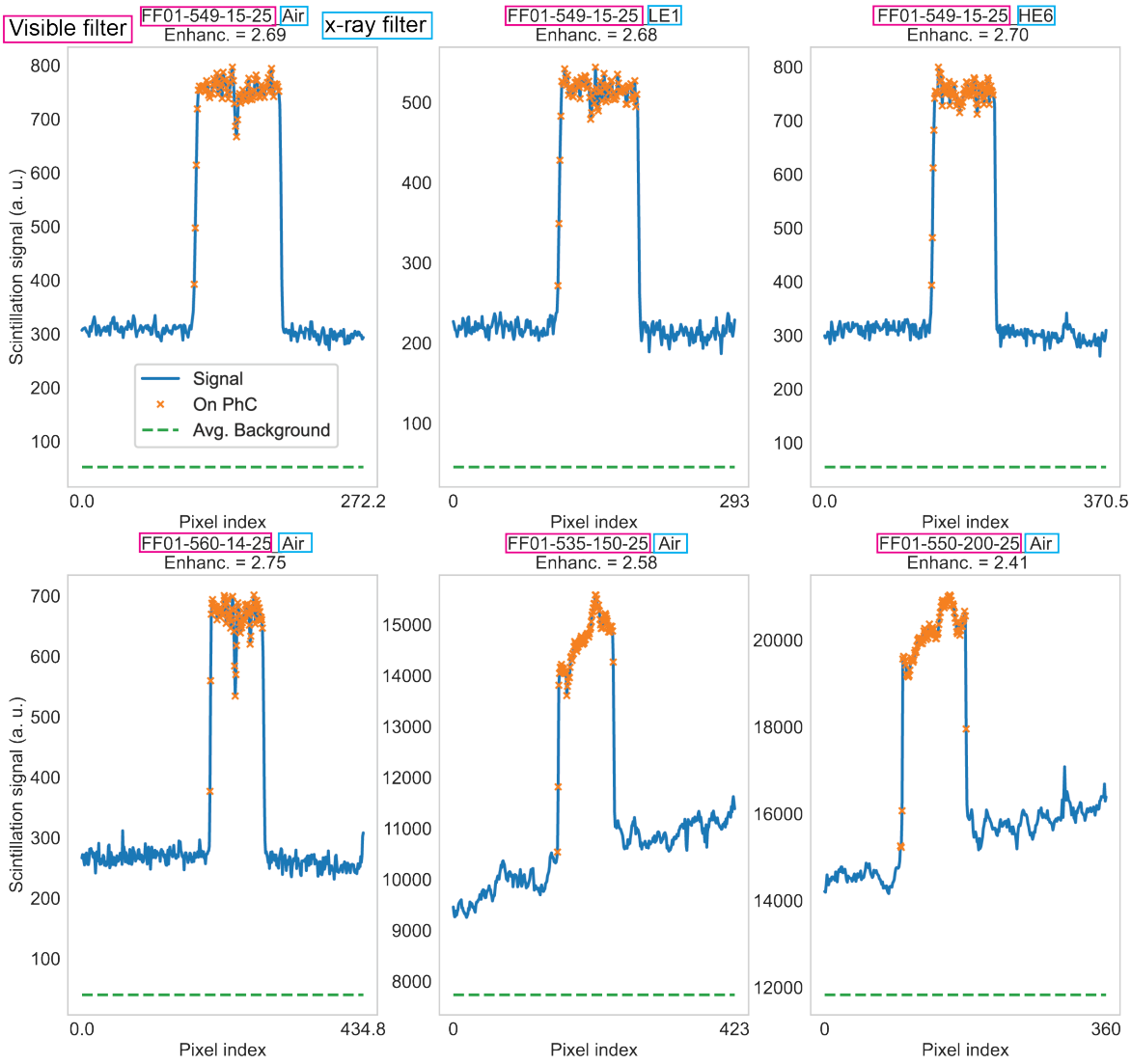

Fig. S15: **Additional scintillation measurement enhancements for various x-ray filters.** Measured sample is 100 μm thick with x-ray source settings: 60 kVp x-ray energy, 5 W emitted x-ray power.

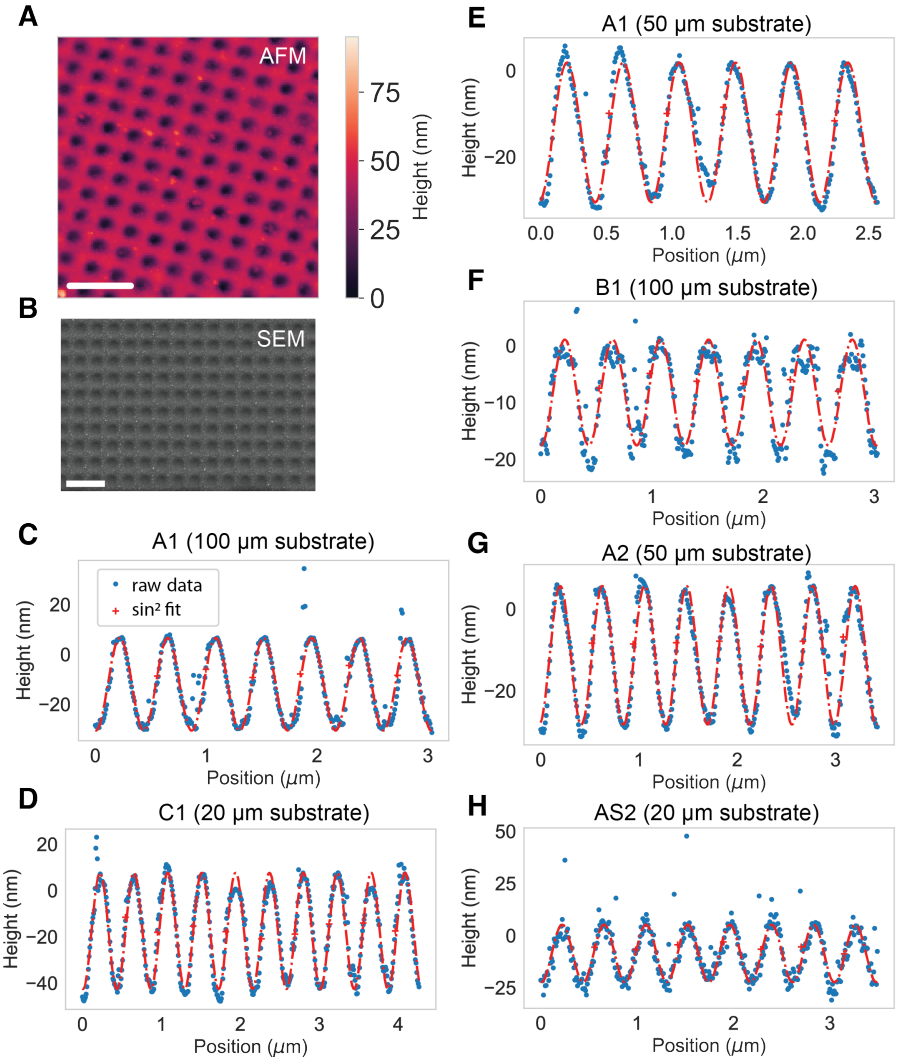

Fig. S16: **Additional sample characterization.** Atomic force microscopy (AFM) and scanning electron microscope (SEM) measurements of various patterned YAG:Ce scintillators. (**A**) 2D AFM measurement of sample A11. Scale bar 1 μm. (**B**) SEM image of sample A2 (on 50 μm thick scintillator). Scale bar 1 μm. (**C-H**) AFM data cuts through the center of a few holes of the patterned area for various samples.

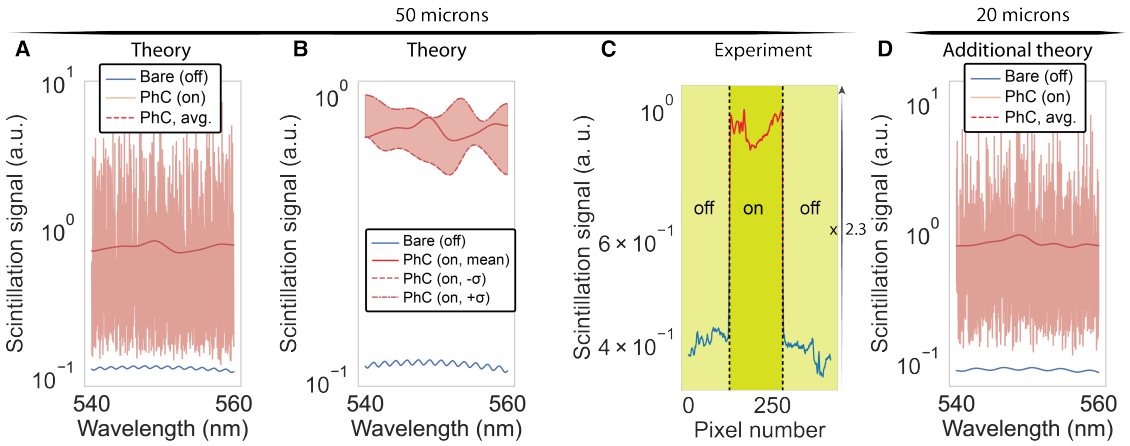

Fig. S17: **Additional x-ray scintillation experimental and numerical results.** (**A**) Predicted scintillation spectrum for sample A2 ($50\ \mu$m). The sharp peaks correspond to narrow resonances of the PhC (which allow free-spectral range due to the thick crystal). (**B**) Influence of parameter uncertainty (here, depth) on the predicted "mean" signal, which is computed by convolving the distribution of (**A**) with a filter of 1.33 nm width. The simulated depths are of 34 $\pm\sigma$ with $\sigma \approx 10$ nm is the uncertainty in the hole-depth of the PhC. (**C**) Measurement scintillation signal along a line of sample A2 ($50\ \mu$m). The measured enhancement is of 2.3. (**D**) Same as (**A**) but for sample C1 ($20\ \mu$m). Signals were recorded with x-ray source settings: (**C**) 60 kVp x-ray energy, 5 W emitted x-ray power.

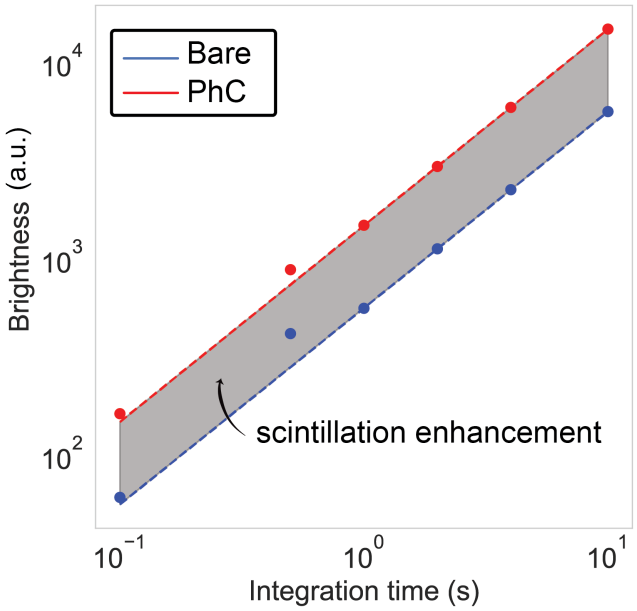

Fig. S18: **Brightness scaling comparison for PhC and bare samples**. This shows that the same integrated signal can be captured over a smaller integration time for the nanophotonic scintillator compared to the unpatterned (bare) scintillator. Measured sample is A1 with x-ray source settings: 60 kVp x-ray energy, 5 W emitted x-ray power.

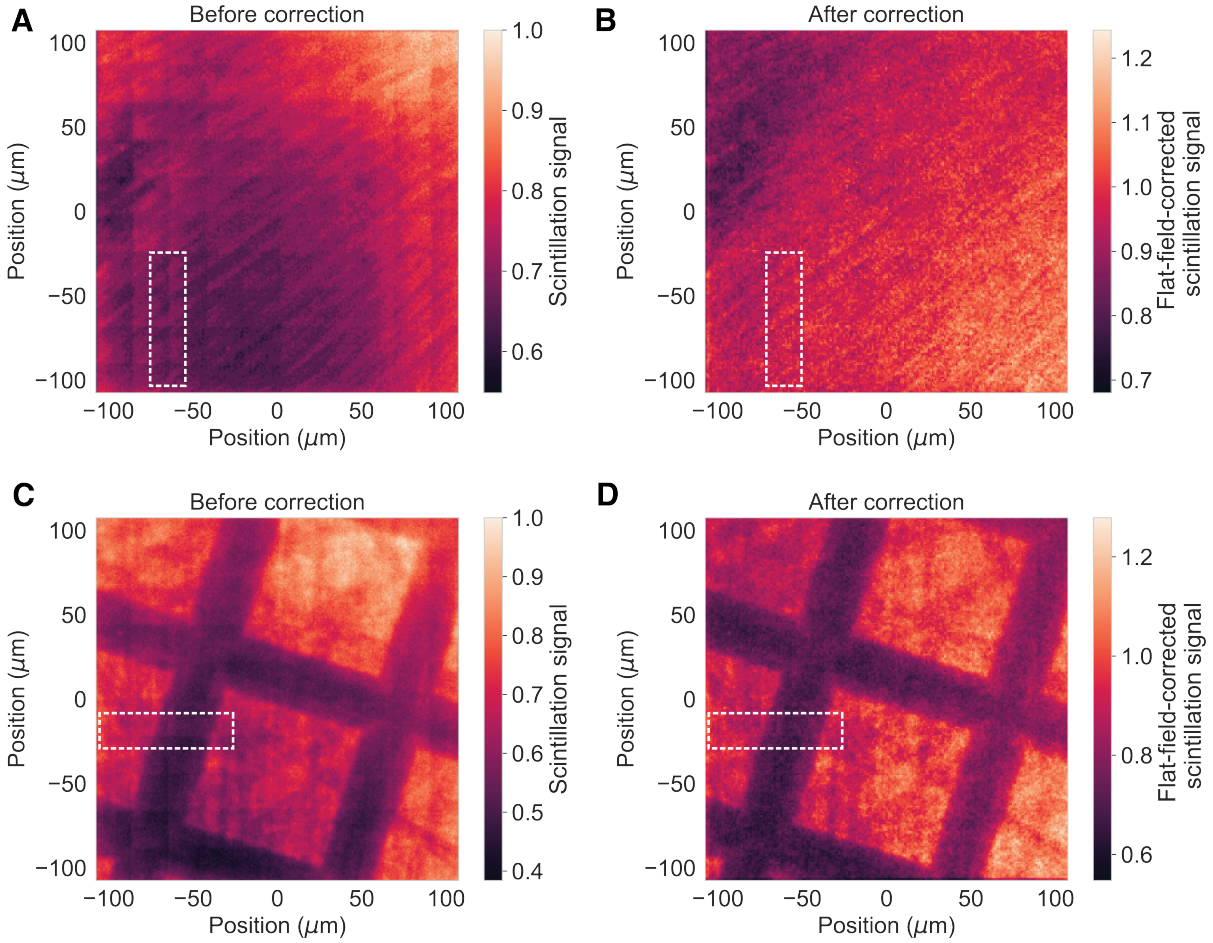

Fig. S19: **X-ray imaging flat-field correction to remove stitching artifacts.** (**A**) Bud image before correction. (**B**) Bud image after correction. (**C**) TEM image before correction. (**D**) TEM image after correction. The white squares are to guide the eye in locations where the artifact is clearly visible in the original image, but was removed by the flat-field correction.

Supplementary Tables

Sample (thickness)	A11 (50 μm)	A12 (50 μm)	A2 (50 μm)	AS2 (50 μm)	A1 (100 μm)	B1 (100 μm)	C1 (20 μm)
Measured enhancement	2.39	2.58	2.31	1.70	2.85	1.50	9.1
Holes diameter (nm)	222	222	200	221	234	192	195
Holes depth (nm)	32	32	34	28	37	19	50
Patterned area (μm $\times$ μm)	215×215	215×215	430×430	430×430	215×215	215×215	215×215
Wafer number	Wafer 1	Wafer 1	Wafer 1	Wafer 3	Wafer 2	Wafer 2	Wafer 4

Table S1: **Compiled x-ray scintillation enhancement experimental results.** The first letter of the sample name indicates the FIB dose used for patterning. Holes diameters and depths are measured with AFM.

References and Notes

1. A. Gektin, M. Korzhik, *Inorganic Scintillators for Detector Systems* (Springer, 2017).

2. S. Cherry, J. Sorenson, M. Phelps, *Physics in Nuclear Medicine* (Wiley, 2012).

3. Q. Chen, J. Wu, X. Ou, B. Huang, J. Almutlaq, A. A. Zhumekenov, X. Guan, S. Han, L. Liang, Z. Yi, J. Li, X. Xie, Y. Wang, Y. Li, D. Fan, D. B. L. Teh, A. H. All, O. F. Mohammed, O. M. Bakr, T. Wu, M. Bettinelli, H. Yang, W. Huang, X. Liu, All-inorganic perovskite nanocrystal scintillators. *Nature* **561**, 88–93 (2018). doi:10.1038/s41586-018-0451-1 Medline

4. Y. Kurman, A. Shultzman, O. Segal, A. Pick, I. Kaminer, Photonic-Crystal Scintillators: Molding the Flow of Light to Enhance X-Ray and γ-Ray Detection. *Phys. Rev. Lett.* **125**, 040801 (2020). doi:10.1103/PhysRevLett.125.040801 Medline

5. E. Yablonovitch, Inhibited spontaneous emission in solid-state physics and electronics. *Phys. Rev. Lett.* **58**, 2059–2062 (1987). doi:10.1103/PhysRevLett.58.2059 Medline

6. J. D. Joannopoulos, S. G. Johnson, J. N. Winn, R. D. Meade, *Photonic Crystals: Molding the Flow of Light* (Princeton Univ. Press, 2011).

7. M. Pelton, Modified spontaneous emission in nanophotonic structures. *Nat. Photonics* **9**, 427–435 (2015). doi:10.1038/nphoton.2015.103

8. A. Polman, H. A. Atwater, Photonic design principles for ultrahigh-efficiency photovoltaics. *Nat. Mater.* **11**, 174–177 (2012). doi:10.1038/nmat3263 Medline

9. P. Anger, P. Bharadwaj, L. Novotny, Enhancement and quenching of single-molecule fluorescence. *Phys. Rev. Lett.* **96**, 113002 (2006). doi:10.1103/PhysRevLett.96.113002 Medline

10. J. B. Jackson, N. J. Halas, Surface-enhanced Raman scattering on tunable plasmonic nanoparticle substrates. *Proc. Natl. Acad. Sci. U.S.A.* **101**, 17930–17935 (2004). doi:10.1073/pnas.0408319102 Medline

11. E. F. Schubert, N. E. J. Hunt, M. Micovic, R. J. Malik, D. L. Sivco, A. Y. Cho, G. J. Zydzik, Highly efficient light-emitting diodes with microcavities. *Science* **265**, 943–945 (1994). doi:10.1126/science.265.5174.943 Medline

12. A. A. Erchak, D. J. Ripin, S. Fan, P. Rakich, J. D. Joannopoulos, E. P. Ippen, G. S. Petrich, L. A. Kolodziejski, Enhanced coupling to vertical radiation using a two-dimensional photonic crystal in a semiconductor light-emitting diode. *Appl. Phys. Lett.* **78**, 563–565 (2001). doi:10.1063/1.1342048

13. J.-J. Greffet, R. Carminati, K. Joulain, J.-P. Mulet, S. Mainguy, Y. Chen, Coherent emission of light by thermal sources. *Nature* **416**, 61–64 (2002). doi:10.1038/416061a Medline

14. R. Remez, N. Shapira, C. Roques-Carmes, R. Tirole, Y. Yang, Y. Lereah, M. Soljačić, I. Kaminer, A. Arie, Spectral and spatial shaping of Smith-Purcell radiation. *Phys. Rev. A* **96**, 061801 (2017). doi:10.1103/PhysRevA.96.061801

15. Y. Yang, A. Massuda, C. Roques-Carmes, S. E. Kooi, T. Christensen, S. G. Johnson, J. D. Joannopoulos, O. D. Miller, I. Kaminer, M. Soljačić, Maximal spontaneous photon emission and energy loss from free electrons. *Nat. Phys.* **14**, 894–899 (2018). doi:10.1038/s41567-018-0180-2

16. I. Kaminer, S. E. Kooi, R. Shiloh, B. Zhen, Y. Shen, J. J. López, R. Remez, S. A. Skirlo, Y. Yang, J. D. Joannopoulos, A. Arie, M. Soljačić, Spectrally and Spatially Resolved Smith-Purcell Radiation in Plasmonic Crystals with Short-Range Disorder. *Phys. Rev. X* **7**, 011003 (2017). doi:10.1103/PhysRevX.7.011003

17. C. Roques-Carmes, S. E. Kooi, Y. Yang, A. Massuda, P. D. Keathley, A. Zaidi, Y. Yang, J. D. Joannopoulos, K. K. Berggren, I. Kaminer, M. Soljačić, Towards integrated tunable all-silicon free-electron light sources. *Nat. Commun.* **10**, 3176 (2019). doi:10.1038/s41467-019-11070-7 Medline

18. F. Liu, L. Xiao, Y. Ye, M. Wang, K. Cui, X. Feng, W. Zhang, Y. Huang, Integrated Cherenkov radiation emitter eliminating the electron velocity threshold. *Nat. Photonics* **11**, 289–292 (2017). doi:10.1038/nphoton.2017.45

19. A. Massuda, C. Roques-Carmes, Y. Yang, S. E. Kooi, Y. Yang, C. Murdia, K. K. Berggren, I. Kaminer, M. Soljačić, Smith-Purcell radiation from low-energy electrons. *ACS Photonics* **5**, 3513–3518 (2018). doi:10.1021/acsphotonics.8b00743

20. F. J. García de Abajo, Optical excitations in electron microscopy. *Rev. Mod. Phys.* **82**, 209–275 (2010). doi:10.1103/RevModPhys.82.209

21. G. Li, B. P. Clarke, J.-K. So, K. F. MacDonald, N. I. Zheludev, Holographic free-electron light source. *Nat. Commun.* **7**, 13705 (2016). doi:10.1038/ncomms13705 Medline

22. C. I. Osorio, T. Coenen, B. J. M. Brenny, A. Polman, A. F. Koenderink, Angle-Resolved Cathodoluminescence Imaging Polarimetry. *ACS Photonics* **3**, 147–154 (2015). doi:10.1021/acsphotonics.5b00596

23. Y. Yang *et al*., Observation of enhanced free-electron radiation from photonic flatband resonances. arXiv 2110.03550 (2021).

24. X. Chen, B. Liu, Q. Wu, Z. Zhu, J. Zhu, M. Gu, H. Chen, J. Liu, L. Chen, X. Ouyang, Enhanced light extraction of plastic scintillator using large-area photonic crystal structures fabricated by hot embossing. *Opt. Express* **26**, 11438–11446 (2018). doi:10.1364/OE.26.011438 Medline

25. A. Knapitsch, E. Auffray, C. W. Fabjan, J.-L. Leclercq, X. Letartre, R. Mazurczyk, P. Lecoq, Results of Photonic Crystal Enhanced Light Extraction on Heavy Inorganic Scintillators. *IEEE Trans. Nucl. Sci.* **59**, 2334–2339 (2012). doi:10.1109/TNS.2012.2184556

26. A. Knapitsch, P. Lecoq, Review on photonic crystal coatings for scintillators. *Int. J. Mod. Phys. A* **29**, 1430070 (2015). doi:10.1142/S0217751X14300701

27. Z. Zhu, S. Wu, C. Xue, J. Zhao, L. Wang, Y. Wu, B. Liu, C. Cheng, M. Gu, H. Chen, R. Tai, Enhanced light extraction of scintillator using large-area photonic crystal structures fabricated by soft-X-ray interference lithography. *Appl. Phys. Lett.* **106**, 241901 (2015). doi:10.1063/1.4922699

28. P. Pignalosa, B. Liu, H. Chen, H. Smith, Y. Yi, Giant light extraction enhancement of medical imaging scintillation materials using biologically inspired integrated nanostructures. *Opt. Lett.* **37**, 2808 (2012). doi:10.1364/OL.37.002808 Medline

29. Z. Zhu, B. Liu, F. Zhang, H. Tang, J. Xu, M. Gu, C. Zhang, L. Chen, J. Liu, X. Ouyang, Improved light output from thick β-Ga_2O_3 scintillation crystals via graded-refractive-index photonic crystals. *Opt. Express* **29**, 18646 (2021). doi:10.1364/OE.428671 Medline

30. X. Ouyang, B. Liu, X. Xiang, L. Chen, M. Xu, X. Song, J. Ruan, J. Liu, C. Chen, Z. Zhu, Y. Li, Enhanced light output of CsI(Na) scintillators by photonic crystals. *Nucl. Instrum. Methods Phys. Res. A* **969**, 164007 (2020). doi:10.1016/j.nima.2020.164007

31. C. A. Klein, Bandgap Dependence and Related Features of Radiation Ionization Energies in Semiconductors. *J. Appl. Phys.* **39**, 2029 (1968). doi:10.1063/1.1656484

32. A. Polman, M. Kociak, F. J. García de Abajo, Electron-beam spectroscopy for nanophotonics. *Nat. Mater.* **18**, 1158–1171 (2019). doi:10.1038/s41563-019-0409-1 Medline

33. P. Wurfel, The chemical potential of radiation. *J. Phys. C* **15**, 3967–3985 (1982). doi:10.1088/0022-3719/15/18/012

34. J. J. Greffet, P. Bouchon, G. Brucoli, F. Marquier, Light Emission by Nonequilibrium Bodies: Local Kirchhoff Law. *Phys. Rev. X* **8**, 021008 (2018). doi:10.1103/PhysRevX.8.021008

35. D. L. Sounas, A. Alù, Non-reciprocal photonics based on time modulation. *Nat. Photonics* **11**, 774–783 (2017). doi:10.1038/s41566-017-0051-x

36. L. Zhu, S. Fan, Persistent Directional Current at Equilibrium in Nonreciprocal Many-Body Near Field Electromagnetic Heat Transfer. *Phys. Rev. Lett.* **117**, 134303 (2016). doi:10.1103/PhysRevLett.117.134303 Medline

37. D. L. C. Chan, M. Soljacić, J. D. Joannopoulos, Direct calculation of thermal emission for three-dimensionally periodic photonic crystal slabs. *Phys. Rev. E* **74**, 036615 (2006). doi:10.1103/PhysRevE.74.036615 Medline

38. This issue is compounded by the sensitivity of the results to assumptions about the spatial and spectral distributions of the dipoles, which are related to the microscopic details of the defect electronic structure, as well as the mechanism of high-energy particle energy transfer into the material.

39. See supplementary materials.

40. H. Demers, N. Poirier-Demers, A. R. Couture, D. Joly, M. Guilmain, N. de Jonge, D. Drouin, Three-dimensional electron microscopy simulation with the CASINO Monte Carlo software. *Scanning* **33**, 135–146 (2011). doi:10.1002/sca.20262 Medline

41. S. Girard, A. Alessi, N. Richard, L. Martin-Samos, V. De Michele, L. Giacomazzi, S. Agnello, D. D. Francesca, A. Morana, B. Winkler, I. Reghioua, P. Paillet, M. Cannas, T. Robin, A. Boukenter, Y. Ouerdane, Overview of radiation induced point defects in silica-based optical fibers. *Rev. Phys.* **4**, 100032 (2019). doi:10.1016/j.revip.2019.100032

42. In principle, one would want to compare V_{eff} in the TF to a "truly intrinsic" or "bulk" silica case. In that case, one would compare to silica of the same thickness (1000 nm). However, because this reference case is a thin film as well, nanophotonic shaping effects in the spectrum will inevitably be present. Comparing the V_{eff} in the thin-film case of Fig. 2 to thin films without (i) the top Si layer or (ii) without both Si layers (see fig. S1), one finds that the TF of Fig. 2 presents slightly smaller absorption enhancement at the red peak, possibly due to the high reflectivity of the top Si layer (suppressing the amount of field that can be absorbed by the material). However, the PhC sample still shows strong shaping and enhancement relative to all TF cases.

43. P. Lecoq, C. Morel, J. O. Prior, D. Visvikis, S. Gundacker, E. Auffray, P. Križan, R. M. Turtos, D. Thers, E. Charbon, J. Varela, C. de La Taille, A. Rivetti, D. Breton, J.-F. Pratte, J. Nuyts, S. Surti, S. Vandenberghe, P. Marsden, K. Parodi, J. M. Benlloch, M. Benoit, Roadmap toward the 10 ps time-of-flight PET challenge. *Phys. Med. Biol.* **65**, 21RM01 (2020). doi:10.1088/1361-6560/ab9500 Medline

44. E. Yablonovitch, Statistical ray optics. *J. Opt. Soc. Am.* **72**, 899 (1982). doi:10.1364/JOSA.72.000899

45. P. Campbell, M. A. Green, The limiting efficiency of silicon solar cells under concentrated sunlight. *IEEE Trans. Electron Dev.* **33**, 234–239 (1986). doi:10.1109/T-ED.1986.22472

46. R. N. Raman, M. J. Matthews, J. J. Adams, S. G. Demos, Monitoring annealing via CO_2 laser heating of defect populations on fused silica surfaces using photoluminescence microscopy. *Opt. Express* **18**, 15207–15215 (2010). doi:10.1364/OE.18.015207 Medline

47. Z. Yu, A. Raman, S. Fan, Fundamental limit of nanophotonic light trapping in solar cells. *Proc. Natl. Acad. Sci. U.S.A.* **107**, 17491–17496 (2010). doi:10.1073/pnas.1008296107 Medline

48. A. I. Zhmakin, Enhancement of light extraction from light emitting diodes. *Phys. Rep.* **498**, 189–241 (2011). doi:10.1016/j.physrep.2010.11.001

49. S. Derenzo, E. Bourret, C. Frank-Rotsch, S. Hanrahan, M. Garcia-Sciveres, How silicon and boron dopants govern the cryogenic scintillation properties of N-type GaAs. *Nucl. Instrum. Methods Phys. Res. A* **989**, 164957 (2021). doi:10.1016/j.nima.2020.164957

50. S. Liu, A. Vaskin, S. Addamane, B. Leung, M.-C. Tsai, Y. Yang, P. P. Vabishchevich, G. A. Keeler, G. Wang, X. He, Y. Kim, N. F. Hartmann, H. Htoon, S. K. Doorn, M. Zilk, T. Pertsch, G. Balakrishnan, M. B. Sinclair, I. Staude, I. Brener, Light-Emitting Metasurfaces: Simultaneous Control of Spontaneous Emission and Far-Field Radiation. *Nano Lett.* **18**, 6906–6914 (2018). doi:10.1021/acs.nanolett.8b02808 Medline

51. K. M. Schulz, D. Jalas, A. Y. Petrov, M. Eich, Reciprocity approach for calculating the Purcell effect for emission into an open optical system. *Opt. Express* **26**, 19247–19258 (2018). doi:10.1364/OE.26.019247 Medline

52. Y. Sheng, W. Wang, R. Shiloh, V. Roppo, Y. Kong, A. Arie, W. Krolikowski, Čerenkov third-harmonic generation in $\chi^{(2)}$ nonlinear photonic crystal. *Appl. Phys. Lett.* **98**, 241114 (2011). doi:10.1063/1.3602312

53. S. Zhang, E. R. Martins, A. G. Diyaf, J. I. B. Wilson, G. A. Turnbull, I. D. W. Samuel, Calculation of the emission power distribution of microstructured OLEDs using the reciprocity theorem. *Synth. Met.* **205**, 127–133 (2015). doi:10.1016/j.synthmet.2015.03.035

54. A. C. Overvig, S. A. Mann, A. Alù, Thermal Metasurfaces: Complete Emission Control by Combining Local and Nonlocal Light-Matter Interactions. *Phys. Rev. X* **11**, 021050 (2021). doi:10.1103/PhysRevX.11.021050

55. S. Molesky, Z. Lin, A. Y. Piggott, W. Jin, J. Vucković, A. W. Rodriguez, Inverse design in nanophotonics. *Nat. Photonics* **12**, 659–670 (2018). doi:10.1038/s41566-018-0246-9

56. A. G. Polimeridis, M. T. H. Reid, W. Jin, S. G. Johnson, J. K. White, A. W. Rodriguez, Fluctuating volume-current formulation of electromagnetic fluctuations in inhomogeneous media: Incandescence and luminescence in arbitrary geometries. *Phys. Rev. B* **92**, 134202 (2015). doi:10.1103/PhysRevB.92.134202

57. W. Yao, F. Verdugo, R. E. Christiansen, S. G. Johnson, Trace formulation for photonic inverse design with incoherent sources. arXiv 2111.13046 (2021).

58. R. E. Christiansen, J. Michon, M. Benzaouia, O. Sigmund, S. G. Johnson, Inverse design of nanoparticles for enhanced Raman scattering. *Opt. Express* **28**, 4444–4462 (2020). doi:10.1364/OE.28.004444 Medline

59. K. Watanabe, T. Taniguchi, T. Niiyama, K. Miya, M. Taniguchi, Far-ultraviolet plane-emission handheld device based on hexagonal boron nitride. *Nat. Photonics* **3**, 591–594 (2009). doi:10.1038/nphoton.2009.167

60. C. Roques-Carmes *et al*., Data for "A framework for scintillation in nanophotonics" (2021); https://github.com/charlesrc/nanoscint.

61. R. Sundararaman, K. Letchworth-Weaver, K. A. Schwarz, D. Gunceler, Y. Ozhabes, T. A. Arias, JDFTx: Software for joint density-functional theory. *SoftwareX* **6**, 278–284 (2017). doi:10.1016/j.softx.2017.10.006 Medline

62. C. Freysoldt, S. Boeck, J. Neugebauer, Direct minimization technique for metals in density functional theory. *Phys. Rev. B* **79**, 241103 (2009). doi:10.1103/PhysRevB.79.241103

63. A. D. Boese, J. M. L. Martin, Development of density functionals for thermochemical kinetics. *J. Chem. Phys.* **121**, 3405–3416 (2004). doi:10.1063/1.1774975 Medline

64. R. Sundararaman, T. A. Arias, Regularization of the Coulomb singularity in exact exchange by Wigner-Seitz truncated interactions: Towards chemical accuracy in nontrivial systems. *Phys. Rev. B* **87**, 165122 (2013). doi:10.1103/PhysRevB.87.165122

65. J. P. Perdew, K. Burke, M. Ernzerhof, Generalized Gradient Approximation Made Simple. *Phys. Rev. Lett.* **77**, 3865–3868 (1996). doi:10.1103/PhysRevLett.77.3865 Medline

66. C. Rackauckas, Q. Nie, DifferentialEquations.jl – A Performant and Feature-Rich Ecosystem for Solving Differential Equations in Julia. *J. Open Res. Softw.* **5**, 15 (2017). doi:10.5334/jors.151

67. V. Liu, S. Fan, S^4: A free electromagnetic solver for layered periodic structures. *Comput. Phys. Commun.* **183**, 2233–2244 (2012). doi:10.1016/j.cpc.2012.04.026

68. W. Jin, W. Li, M. Orenstein, S. Fan, Inverse Design of Lightweight Broadband Reflector for Relativistic Lightsail Propulsion. *ACS Photonics* **7**, 2350–2355 (2020). doi:10.1021/acsphotonics.0c00768

69. S. Johnson, The NLopt nonlinear-optimization package (2014).

70. K. Watanabe, T. Taniguchi, H. Kanda, Direct-bandgap properties and evidence for ultraviolet lasing of hexagonal boron nitride single crystal. *Nat. Mater.* **3**, 404–409 (2004). doi:10.1038/nmat1134 Medline

71. C. Chatterley, K. Linden, Demonstration and evaluation of germicidal UV-LEDs for point-of-use water disinfection. *J. Water Health* **8**, 479–486 (2010). doi:10.2166/wh.2010.124 Medline

72. M. Buonanno, D. Welch, I. Shuryak, D. J. Brenner, Far-UVC light (222 nm) efficiently and safely inactivates airborne human coronaviruses. *Sci. Rep.* **10**, 10285 (2020). doi:10.1038/s41598-020-67211-2 Medline

73. K. Watanabe, T. Taniguchi, Hexagonal boron nitride as a new ultraviolet luminescent material and its application. *Int. J. Appl. Ceram. Technol.* **8**, 977–989 (2011). doi:10.1111/j.1744-7402.2011.02626.x

74. M. Schlipf, F. Gygi, Optimization algorithm for the generation of ONCV pseudopotentials. *Comput. Phys. Commun.* **196**, 36–44 (2015). doi:10.1016/j.cpc.2015.05.011

75. D. L. Griscom, Self-trapped holes in amorphous silicon dioxide. *Phys. Rev. B* **40**, 4224–4227 (1989). doi:10.1103/PhysRevB.40.4224 Medline

76. C. Franchini, M. Reticcioli, M. Setvin, U. Diebold, Polarons in materials. *Nat. Rev. Mater.* **6**, 560–586 (2021). doi:10.1038/s41578-021-00289-w

77. M. A. Marques, M. J. Oliveira, T. Burnus, Libxc: A library of exchange and correlation functionals for density functional theory. *Comput. Phys. Commun.* **183**, 2272–2281 (2012). doi:10.1016/j.cpc.2012.05.007

78. D. L. Griscom, Electron spin resonance characterization of self-trapped holes in amorphous silicon dioxide. *J. Non-Cryst. Solids* **149**, 137–160 (1992). doi:10.1016/0022-3093(92)90062-O

79. D. L. Griscom, Self-trapped holes in pure-silica glass: A history of their discovery and characterization and an example of their critical significance to industry. *J. Non-Cryst. Solids* **352**, 2601–2617 (2006). doi:10.1016/j.jnoncrysol.2006.03.033

80. S. Sicolo, G. Palma, C. Di Valentin, G. Pacchioni, Structure and ESR properties of self-trapped holes in pure silica from first-principles density functional calculations. *Phys. Rev. B* **76**, 075121 (2007). doi:10.1103/PhysRevB.76.075121

81. G. Pacchioni, A. Basile, Calculated spectral properties of self-trapped holes in pure and Ge-doped SiO_2. *Phys. Rev. B* **60**, 9990–9998 (1999). doi:10.1103/PhysRevB.60.9990

82. P. Giannozzi, S. Baroni, N. Bonini, M. Calandra, R. Car, C. Cavazzoni, D. Ceresoli, G. L. Chiarotti, M. Cococcioni, I. Dabo, A. Dal Corso, S. de Gironcoli, S. Fabris, G. Fratesi, R. Gebauer, U. Gerstmann, C. Gougoussis, A. Kokalj, M. Lazzeri, L. Martin-Samos, N. Marzari, F. Mauri, R. Mazzarello, S. Paolini, A. Pasquarello, L. Paulatto, C. Sbraccia, S. Scandolo, G. Sclauzero, A. P. Seitsonen, A. Smogunov, P. Umari, R. M. Wentzcovitch, QUANTUM ESPRESSO: A modular and open-source software project for quantum simulations of materials. *J. Phys. Condens. Matter* **21**, 395502 (2009). doi:10.1088/0953-8984/21/39/395502 Medline